

Chemical abundances in LMC stellar populations

I. The Inner disk sample [★]

Luciana Pompéia¹, Vanessa Hill², Monique Spite², Andrew Cole³, Francesca Primas⁴, Martino Romaniello⁴, Luca Pasquini⁴ Maria-Rosa Cioni⁵ and Tammy Smecker Hane⁶

¹ Instituto Astronômico e Geofísico (USP), Rua do Matão 1226, Cidade Universitária, 05508-900 São Paulo, Brazil

e-mail: pompeia@astro.iag.usp.br

² Observatoire de Paris-Meudon, GEPI and CNRS UMR 8111, 92125 Meudon Cedex, France

e-mail: Vanessa.Hill@obspm.fr e-mail: Monique.Spite@obspm.fr

³ Kapteyn Astronomical Institute, University of Groningen, Postbus 800, NL-9700 AV Groningen, Netherlands

e-mail: cole@astro.rug.nl

⁴ European Southern Observatory, Karl Schwarzschild Str. 2, 85748 Garching b. München, Germany

e-mail: fprimas@eso.org e-mail: mromanie@eso.org e-mail: lpasquin@eso.org

⁵ Edinburg SUPA, School of Physics, University of Edinburgh, IfA, Blackford Hill, Edinburgh EH9 3HJ, UK

e-mail: mrc@roe.ac.uk

⁶ Department of Physics and Astronomy, 4129 Frederick Reines Hall, University of California, Irvine, CA 92697-4575

e-mail: smecker@carina.ps.uci.edu

Received/Accepted

Abstract. The advent of the new class 8 meters telescopes allows for the first time the detailed study of numerous stars of galaxies other than our own. The Large Magellanic Cloud is one of the most interesting targets due to its proximity and its relatively face-on disk, permitting to separate populations pertaining to the different structures of the galaxy. We have used FLAMES (the Fibre Large Array Multi Element Spectrograph) at the VLT-UT2 telescope to obtain spectra of a large sample of stars from the Inner Disk of the LMC, ~ 2 kpc from the center of the galaxy. We investigate the chemical abundances of iron-peak elements, heavy and light *s*-process elements, Cu, Na, Sc and α -elements for a sample of red giant

stars. Metallicities for the sample stars range from $[\text{Fe}/\text{H}] = -1.7$ to -0.3 . LMC inner disk stars show a definitely different chemical pattern when compared to galactic stars of the same metallicity. The α -elements Ca, Si and Ti show lower $[\text{X}/\text{Fe}]$ ratios relative to Galactic stars, with most $[\text{Ca}/\text{Fe}]$ being subsolar. $[\text{O}/\text{Fe}]$ and $[\text{Mg}/\text{Fe}]$ ratios are slightly deficient, with Mg showing some overlap with the Galactic distribution. Sc and Na follow the underabundant behavior of Ca, with subsolar distributions. For the light s -elements Y and Zr, we have found underabundant values compared to their Galactic counterparts, while the heavy s -elements Ba and La show an opposite trend, with supersolar values for most of the stars. Such results are in agreement with those found for the Dwarf Spheroidal Galaxies and the suggestion of a separate r -process site for Y, and here we add, for Zr, both light- s elements. $[\text{La}/\text{Fe}]$ ratios are slightly overabundant relative to the galactic pattern with very low scatter and Ba has a peculiar distribution: for metallicities lower than $[\text{Fe}/\text{H}] \simeq -1.15$ dex the $[\text{Ba}/\text{Fe}]$ ratios decrease with increasing metallicities, while for higher metallicities the distribution shows an increasing trend. The $[\text{heavy-}s/\text{light-}s]$ ratios are high, with a hint for a slow increasing trend with metallicity. A surprising result is found for three of the iron-peak elements. We have found an offset for the $[\text{iron-peak}/\text{Fe}]$ ratios of Ni, Cr and Co with an underabundant pattern and subsolar values, while Vanadium ratios track the solar value. Copper shows a very low abundance in our sample for all metallicities, compatible with those of the Galaxy only for the most metal-poor stars. We have also compared our results with those of the Local Group Dwarf Spheroidal Galaxies, although we can only make a rough comparison because of the paucity of stars in similar metallicity bins, except for the Sagittarius dwarf galaxy (Sgr). The results are the following. Alpha-elements, Na and Sc in the dSph galaxies show similar pattern relative to LMC stars. Compared to the Sgr galaxy data, we found similar distributions for O, Mg, Ca and Si. For the iron-peak elements we found that the LMC stars are midly underabundant relative to the data of the dSph. Finally, the abundance results for the s -process elements indicate that the LMC stars are slightly enhanced compared to stars from the dSph galaxies. The overall chemical distributions of this LMC sample indicates a slower star formation history relative to that of the solar neighborhood, with a higher contribution from Type Ia supernovae relative to Type II supernovae. The picture that has been revealed with the chemical distributions of the Local Group Galaxies, and is supported by our results, indicates a global building scenario instead of a galaxy formation process with accreting events.

Key words. Stars: abundances, Galaxies: Magellanic Clouds, Galaxies: abundances, Galaxies: evolution

1. Introduction

During the last decade, due to the operation of the new class large telescopes, we have been witnessing for the first time the chemical analysis of large samples of individual stars from external galaxies. Thanks to new optical technologies, objects fainter than supergiant stars, planetary nebulae or HII regions are now possible targets to extragalactic research, allowing the study of older objects and the exploration of earlier phases of galaxy evolution. The abundance pattern of diverse elements in numerous stars in a galaxy give information on different domains such as the kinematic and chemical evolutions, the nucleosynthesis of the elements, the star formation history (SFH) and the initial mass function (IMF) of the given population.

One of the most interesting extragalactic objects to the study of stellar populations is the Large Magellanic Cloud (LMC), our nearest companion after the Sagittarius dwarf galaxy, which is in a merging process with the Milky Way. The LMC is an irregular galaxy located within 50 Kpc from the Sun. A disk, a bar and a thick disk or flattened halo have already been kinematically defined in the LMC (e.g. Westerlund 1997). The almost face-on position of its disk, with a tilt relative to the plane of the sky of $\sim 30^\circ$, gives us the precious opportunity to study stars from its different components. An observational project aiming at making the full chemical analysis of significant samples (~ 70 -100) of stars from different locations in the LMC has been developed taking advantage of the FLAMES multiplex facility at the VLT. We have obtained spectra from stars in three different regions of the LMC: the Inner Disk (characterised by a galactocentric radius of $R_C=2\text{kpc}$); the Outer Disk (with $R_C=4\text{kpc}$); and a field near the optical center of the Bar. Stars have been selected based on kinematics and metallicity data derived from the infrared calcium triplet (CaT), trying to sample as evenly as possible the whole metallicity range of this galaxy.

According to models of galaxy formation within a hierarchical CDM scenario (D’Onghia & Lake 2004, Moore et al. 1999), the past history of the Milky Way galaxy is closely connected to its environment. Particularly, the Magellanic Clouds, as the nearest galaxies and with a strong evidence of ancient dynamical interaction with the Galaxy, may preserve important clues about the formation and evolution of the Milky Way. In the present paper we focus on the Inner Disk region and we present abundance results for iron-peak, heavy and light *s*-process elements, and α elements for the Inner Disk stars in a total of 62 stars. With this detailed information in hands, we aim at shedding light on the following questions: (i) what are the chemical distributions of the Inner Disk of the LMC?; (ii) what do these chemical distributions tell us about the formation and

Send offprint requests to: L. Pompeia, e-mail: pompéia@astro.iag.usp.br

* Based on observations collected at the VLT UT2 telescope (072.B-0608 and 066.B-0331 programs), Chile.

evolution of the LMC?; (iii) are they similar to any other component of the Milky Way?; (iv) or to the populations of other Local Group galaxies?; (v) from the chemical point of view, is a merging scenario with LMC debris a likely solution for the Galactic Halo formation?

The paper is organized as follows: in Sect. 2 the observations and the reduction procedure are described; in Sect. 3 the stellar parameters calculation is presented; Sect. 4 describes the abundance determination procedures; Sect. 5 reports the results for the abundance ratios, comparing to samples of the Galaxy; in Sect. 6 we compare our results to those for the dSph galaxies; we discuss the results in Sect. 7; and finally in Sect. 8 a summary of the work is given.

2. Sample selection, observations and reductions

2.1. Sample selection

To best measure the chemical abundances of the LMC disk and their evolution along time, we selected a field located 1.7° southwest of the LMC Bar, in the Bar's minor axis direction which ensures a negligible contribution of the Bar's stellar populations. This field was already studied photometrically from HST color-magnitude diagrams (Smecker-Hane et al. 2002, hereafter SMH02), indicating that the star formation history has been rather smooth and continuous over the last 15 Gyrs, with a possible slight enhancement in the last 2 Gyrs (contrary to the recent enhanced star formation episodes detected in the LMC Bar between 4 and 6 Gyrs). This field has also more recently been the target of a low-resolution spectroscopy campaign (Smecker-Hane et al. in press, hereafter SMH), around the infrared calcium triplet (CaT), to derive its metallicity distribution and a relatively flat age-metallicity relation.

We have used these infrared CaT metallicities from SMH to select a sample of red giant branch stars members of the LMC (based on their radial velocities) and distributed uniformly (i.e. with the same number of stars in each metallicity bin) over the whole metallicity range of the LMC disk. In this way, we have been able to sample very efficiently also the lower metallicity bins of the LMC. The most metal-poor stars convey essential information on the chemical evolution of this galaxy, but they are rare, hence their number would have been significantly lower if we would have selected our sample by picking stars randomly across the RGB. The final sample consists in 67 stars with CaT metallicities ranging from -1.76 to -0.02 dex (including 13 stars with metallicities below -1.0 dex), drawn from the 115 stars sample of SMH. In Fig. 1 we show the sample stars overplotted on the color-magnitude diagram of the LMC disk region targetted (CTIO photometry from SMH). As can be seen from this figure, the sample mean magnitude is around $V=17.25$ mag, bright enough to allow reasonable S/N high-resolution spectra to be acquired.

2.2. Observations and reductions

The observations were made at the VLT Kueyen (UT2) telescope at Paranal during the Science Verification of FLAMES/GIRAFFE (Pasquini et al. 2000) in January, February and March, 2003, complemented by one night of the Paris Observatory Guaranteed Time Observations in January, 2004. In its MEDUSA mode, GIRAFFE is a multiobject spectrograph with 131 fibers of which 67 were used for the present project¹. The detector is a 2048 X 4096 EEV CCD with 15 μ m pixels. We used the high resolution grating of GIRAFFE in three different setups: (i) H14 λ 638.3 - λ 662.6 nm with R=28800; (ii) H13 λ 612.0 - λ 640.6 nm with R=22500, and (iii) H11 λ 559.7 - λ 584.0 nm with R=18529. Exposure times are 6 hours for H14 and H13 setups and 7h30 for H11. The setups were chosen in order to cover the maximum number of key elements such as Fe I and Fe II for spectroscopic calculations of stellar parameters, and α , iron-peak and *s* process elements, for chemical evolution analysis. The average signal to noise ratio of the spectra is S/N \sim 40 per pixel.

The data reduction was carried out using the BLDRS (GIRAFFE Base-Line Data Reduction Software <http://girbldrs.sourceforge.net/>) and consists of bias subtraction, localization and extraction of the spectra, wavelength calibration and rebinning. We have also used the MIDAS packages for sky subtraction and co-addition of individual exposures.

3. Determination of stellar parameters

3.1. Photometric stellar parameters

A first guess of the stellar parameters was made from photometric data of CTIO (V,I from SHM) and 2MASS (J,H,K). Bolometric magnitudes and effective temperatures were derived from calibrations of Bessell, Castelli & Plez (1998, hereafter BCP). The observed CTIO and 2MASS colors were transformed into the corresponding photometric systems using Fernie (1983, V–I Cousins to Johnson) and Carpenter (2001, K, V–K & J–K 2MASS). Photometric data are given in Table 1, while Table 2 gives the derived effective temperatures (T_{phot}) and gravities ($\log g_{\text{phot}}$): T_{phot} is derived using the BCP calibration of the dereddened V–I and V–K colors, and the gravity is computed using the following relation:

$$\log g_{\text{phot}} = 4.44 + \log(M) + 4 \times \log(T_{\text{phot}}/5790.) + 0.4 \times (M_{\text{bol}} - 4.75),$$

where M_{bol} is computed from the dereddened K magnitude of the star, the bolometric correction BC_K taken from BCP and a distance modulus to the LMC of 18.5 mag, and the mass of the stars (M) are assumed to be $2M_{\odot}$. For the reddening, two values

¹ The remaining fibers were allocated to targets of other Science Verification projects in the LMC

were checked: $E(B-V) = 0.03$, was derived by SMH02 for the sample of the Inner Disk, using Strömgren photometry, whereas $E(B-V) = 0.06$, a mean value for the whole disk (Bessell 1991).

We adopted CaT metallicities from SMH as our initial guesses and reported them in the $[Fe/H]_{CaT}$ column of Table 2.

3.1.1. Temperatures

We have derived temperatures from V-I, V-K and J-K colors. We have found some trends when comparing temperatures from different colors: $T_{\text{eff}}(V-I)$ is 65K hotter than $T_{\text{eff}}(V-K)$ in the mean, with $\sigma=59K$; $T_{\text{eff}}(J-K)$ is 21K hotter than $T_{\text{eff}}(V-K)$ and shows a highly dispersed relation, with $\sigma=118K$ (these numbers vary only slightly when using a reddening of $E(B-V)=0.06$ or 0.03). As initial values of our stellar temperatures we have chosen to use a weighted mean (of the different estimates mentioned above), leaving out the less temperature sensitive (J-K) color index and giving a higher weight to the most temperature sensitive (V-K), according to the following expression:

$$T_{\text{eff}} = (T_{\text{eff}}(V-I) + 2 \times T_{\text{eff}}(V-K))/3.$$

In Table 2 the inferred temperatures for the two values of reddening, T_{photLow} and T_{phot} for $E(B-V) = 0.03$ and 0.06 respectively, are given.

3.2. Spectroscopic parameters

The final stellar parameters used for abundance determination of the sample stars were derived spectroscopically in the following way, using abundances derived from the equivalent widths (EW) of iron lines. We have estimated the stellar parameters as follows: effective temperatures are calculated by requiring no slope in the $A(\text{Fe I})$ vs. χ_{exc} graphic; microturbulent velocities, V_t , are derived demanding that lines of different EW give the same iron abundance; and gravities are determined by forcing the agreement between Fe I and Fe II iron abundances (within the accuracy of the abundance determination of Fe II). For the temperature and gravity ranges covered by our current sample of stars, T_{eff} and $\log g$ determinations are well correlated and the calculation of stellar parameters is made iteratively. In Fig. 2 we show an example of the excitation and ionization equilibrium calculations for the star RGB_625, with plots of $A(\text{FeI})$ vs. χ_{exc} and $A(\text{FeI})$ vs. EW. The spectroscopic and photometric parameters of all our stars are reported in Table 2, together with the barycentric radial velocities calculated from the spectra.

3.2.1. Equivalent widths, line list and model atmospheres

The EW of the lines and the radial velocities (Rv, reported in Table 2) of the stars are computed using the program DAOSPEC written by Stetson (Stetson and Pancino, in

preparation). The line list and the atomic data were assembled from the literature and the log gf references are given in Table 3

The model atmospheres are OSMARCS models kindly provided by Plez (private communication 1993-1995, described in Plez & Brett 1992, and 2000, described in Cayrel et al. 2004).

3.2.2. Comparison with UVES analysis

In a previous observing run (066.B-0331), we had obtained UVES spectra (in slit mode) for two of our sample stars, RGB_666 and RGB_808. UVES is an echelle spectrograph also mounted on the VLT Kueyen telescope with a higher resolving power: $R = 45000$ (with a slit of $1''$) and a much wider wavelength coverage (in the case of our chosen setup, 4800-6800Å), and therefore with a better performance to derive equivalent widths. In Fig. 3, equivalent widths derived with DAOSPEC from UVES spectra are compared to those measured on the GIRAFFE spectra of the same 2 stars (left plot: RGB_666, right plot: RGB_808). In the left upper corner of the graphics, the mean difference of both analyses are given together with the dispersion and the number of lines used (lines of all elements are plotted in these comparison). We can see from these plots that GIRAFFE EW are only slightly higher than UVES EW. Such a difference is probably due to a better definition of the continuum for the UVES spectra. The effect is slightly more pronounced for EW larger than 150, but this is expected because of the gaussian approximation with a fixed FWHM made by DAOSPEC when fitting the lines: at UVES resolution, this leads to underestimating the EW of the strongest lines. We have also noticed that the plot for RGB_666 shows a higher scatter, maybe due to the lower temperature of this star.

Comparing the stellar parameters, we have found a good agreement between both analyses, showing that results from GIRAFFE spectra are robust. For RGB_666 the parameters derived from the UVES spectra are: $T_{\text{eff}} = 4300$ K, $\log g = 0.80$ dex, $[\text{Fe}/\text{H}] = -1.10$ dex and $V_t = 1.7$ kms^{-1} , i.e. a difference of $\Delta(T_{\text{eff}}) = 29$ K, $\Delta(\log g) = 0.20$ dex, $\Delta([\text{Fe}/\text{H}]) = 0.08$ dex and $\Delta(V_t) = 0.00$ kms^{-1} compared to the parameters inferred from GIRAFFE spectra. For RGB_808 we have found: $T_{\text{eff}} = 4500$ K, $\log g = 1.00$ dex, $[\text{Fe}/\text{H}] = -1.65$ dex and $V_t = 1.70$ kms^{-1} respectively a difference of $\Delta(T_{\text{eff}}) = 50$ K, $\Delta(\log g) = 0.10$ dex, $\Delta([\text{Fe}/\text{H}]) = 0.17$ dex and $\Delta(V_t) = 0.10$ kms^{-1} .

3.3. Behavior of stellar parameters

We have found good agreement between spectroscopic and photometric temperatures. Our spectroscopic temperatures are hotter than photometric temperatures derived using the low reddening value, T_{photLow} , by 99 K, with $\sigma=63$ K, and by 58K than T_{phot}

(higher reddening value) with $\sigma=64\text{K}$. An interesting result is depicted in Fig. 4 where we compare the spectroscopic temperatures $T_{\text{eff}}(\text{spec})$ with those derived from colors, $T_{\text{eff}}(\text{V-I})$ and $T_{\text{eff}}(\text{V-K})$, and from the equation given in Sect. 3.1.1, $T_{\text{eff}}(\text{Phot})$, for both values of reddening ($E(\text{B-V})=0.06$ in the upper panels, and $E(\text{B-V})=0.03$ in the lower panels). This figure shows that photometric temperatures inferred using $E(\text{B-V}) = 0.06$ are in much better agreement with spectroscopic temperatures than those derived with the lower $E(\text{B-V})$. Provided that the photometric temperatures (of Alonso et al. 1999) and the excitation temperature scales are well aligned, this could indicate that $E(\text{B-V})=0.06$ is a better reddening value for this region.

As a check of the spectroscopic gravities, we have plotted in Fig. 5 the differences between abundances of ionized and neutral species against the abundances of the neutral species for Fe and Ti: $[\text{FeI}/\text{H}] - [\text{FeII}/\text{H}]$ vs. $[\text{FeI}/\text{H}]$ (lower panel) and $[\text{TiI}/\text{H}] - [\text{TiII}/\text{H}]$ vs. $[\text{TiI}/\text{H}]$ (upper panel). This figure shows that when iron satisfies ionization equilibrium (which is our requirement to determine the gravity of our stars), there is also agreement of neutral and ionized titanium (although with a higher scatter and larger error bars due to the smaller number of lines for this element). On average, spectroscopic surface gravities are lower than the photometric estimates by $\Delta(\log g_{\text{spec}} - \log g_{\text{phot}}) = -0.38$ dex, as might be expected if NLTE overionization effects are at work (this systematic effect in $\log g$ corresponds to a 0.2 dex difference between FeI and FeII).

The metallicities that we derive differ from those derived from the CaT by $\Delta([\text{Fe}/\text{H}]_{\text{CaT}} - [\text{Fe}/\text{H}]_{\text{spec}}) = +0.12$ dex with $\sigma = 0.27$ dex. In fact, most of this effect comes from the high-metallicity end of the sample: for $[\text{Fe}/\text{H}]_{\text{CaT}} > -0.6$ dex, CaT seems to overestimate systematically the metallicity by 0.29 dex ($\sigma = 0.17$ dex), whereas for the metal-poor end of the sample, there is almost no systematic effect ($\Delta([\text{Fe}/\text{H}]_{\text{CaT}} - [\text{Fe}/\text{H}]_{\text{spec}}) = -0.06$ dex with $\sigma = 0.22$ dex).

Finally, in Fig. 6, abundance ratios of different species, $[\text{Cr}/\text{Fe}]$, $[\text{Ni}/\text{Fe}]$ and $[\text{V}/\text{Fe}]$, against temperatures are plotted in order to check the quality of the spectroscopic temperatures. As can be seen from this picture, there is no trend of the abundances of the elements with temperatures, which means that our temperatures are well defined. Our final sample comprises 62 red giant stars within $-1.7 < [\text{Fe}/\text{H}] < -0.30$ dex and temperatures ranging from 3900 K to 4500 K. Although 67 stars were observed, 5 of them have one or two setups with low S/N, compromising the stellar parameters determination. These stars have not been included in the analysis.

4. Abundance determination

We have selected a list of lines covering the chosen setups in order to sample as much as possible the most important elements: iron-peak, neutron-capture and α elements. Abundances are derived from EW measurements for seven elements (in parenthesis the average number of lines used in the analysis): Fe (45), Ni (7), Cr (4), V (11), Si (3), Ca (10), Ti (7) and Na (3). We have also derived abundances by using line synthesis for nine elements (in parenthesis the lines used in the synthesis): O ([O I] 6300Å); Mg I (5711 Å), Co I (5647 Å), Cu I (5782 Å), Sc II (5657 Å), La II (6320 Å), Y II (6435 Å), Ba II (6496 Å), and Zr I (6134 Å). The code used for the abundance analysis was developed by Monique Spite (1967) and has been improved along the years. Hyperfine structures (HFS) are taken into account for the following elements (the line sources are given in parenthesis): Ba II (Rutten 1978, and the isotopic solar mix following McWilliam 1998); La II (Lawler et al. 2001 with log gf from Bord et al. 1996); Cu (Biehl 1976); Co I and Sc II (Prochaska et al. 2000). In Fig. 7 the fitting procedure is shown for the Y I 6435Å line in RGB_752 and the La II line 6320Å in RGB_690. Abundances are given relative to solar abundances of Grevesse & Sauval (2000), except for iron and oxygen for which we have adopted $A(\text{Fe}) = 7.50$ and $A(\text{O}) = 8.87$. Atomic lines for the synthesis have been chosen according to the quality of the synthetic fit in the Solar Flux Atlas of Kurucz et al. (1984). For the Sun we have found: $[\text{Mg}/\text{Fe}] = +0.11$ dex; $[\text{Co}/\text{Fe}] = +0.12$ dex; $[\text{Cu}/\text{Fe}] = +0.20$ dex; $[\text{Sc}/\text{Fe}] = 0.00$ dex; $[\text{Ba}/\text{Fe}] = +0.20$ dex; $[\text{Zr}/\text{Fe}] = -0.10$ dex (mean of the two lines); $[\text{Y}/\text{Fe}] = 0.00$ dex; and $[\text{La}/\text{Fe}] = 0.10$ dex. In the following sections we have not corrected our abundance ratios for the values given above. In Tables 4 to 7 the estimated abundances are given.

4.0.1. Abundance Errors

Errors in the estimated abundances have three main sources: the uncertainties in the stellar parameters, the uncertainties in the measurements of the EW (or spectrum synthesis fitting) and the uncertainties on the physical data of the lines (mainly log gf).

The errors due to stellar parameters uncertainties, $\delta([\text{X}/\text{Fe}]_{\text{model}})$, are given in Table 8, assuming the following uncertainties in each of the stellar parameters: $\Delta(T_{\text{eff}}) = \pm 100\text{K}$, $\Delta(\log g) = \pm 0.4$ dex, $\Delta(V_t) = \pm 0.2$ km/s and $\Delta([\text{Fe}/\text{H}]) = \pm 0.15$ dex. Errors in the EW measurement are computed by DAOSPEC during the fitting procedure, then propagated into an abundance uncertainty for each line, and then combined into an abundance error on the mean abundance for each element (δ_{DAOSPEC}). For elements measured by synthesis spectrum fitting, the δ_{DAOSPEC} was replaced by an estimate of the typical abundance change for which two different synthetic spectra (i.e. computed with two slightly different abundances) still fit satisfactorily the same line. On average,

these values are the following for each element: $\delta[\text{Zr}/\text{H}] = 0.15$ dex; $\delta[\text{Y}/\text{H}] = 0.15$ dex; $\delta[\text{La}/\text{H}] = 0.20$ dex; $\delta[\text{Ba}/\text{H}] = 0.25$ dex; $\delta[\text{Co}/\text{H}] = 0.10$ dex; $\delta[\text{Cu}/\text{H}] = 0.20$ dex; $\delta[\text{Sc}/\text{H}] = 0.10$ dex; $\delta[\text{Mg}/\text{H}] = 0.15$ dex and $\delta[\text{O}/\text{H}] = 0.20$ dex. Finally, errors due to the combined uncertainties on the line data and line measurement, are reflected in the abundance dispersion observed for each element, provided that the number of lines is large enough to measure robustly this dispersion ($N \geq 5$). When the number of lines measured is smaller, this error estimate may be substituted by the abundance dispersion observed around iron (the most representative species), assuming that the uncertainties (measurement and line data) responsible for the dispersion are similar for all species. To estimate the final uncertainty on the abundance of each element, we therefore combined these various error estimates in a conservative way, taking the maximum of the following quantities :

$$\begin{aligned} N_X < 3: \quad & \delta([X/H]) = \text{Max}(\delta_{DAOSPEC}, \frac{\sigma(\text{Fe I})}{\sqrt{N_X}}) \\ 3 \leq N_X < 5: \quad & \delta([X/H]) = \text{Max}(\delta_{DAOSPEC}, \frac{\sigma(X)}{\sqrt{N_X}}, \frac{\sigma(\text{Fe I})}{\sqrt{N_X}}) \\ N_X \geq 5: \quad & \delta([X/H]) = \text{Max}(\delta_{DAOSPEC}, \frac{\sigma(X)}{\sqrt{N_X}}), \end{aligned} \quad (1)$$

where N_X is the number of lines of the element X.

Then, in order to estimate the total error in the $[\text{X}/\text{Fe}]$ ratios (measurement error plus error due to the stellar parameter uncertainty), we combined:

$$\delta([X/Fe])_{Tot} = \sqrt{\delta([X/Fe])_{\text{model}}^2 + \delta([X/H])^2 + \delta([\text{Fe}/\text{H}])^2} \quad (2)$$

where $\delta([X/H])$ is the value of equation (1) for element X, $\delta([\text{Fe}/\text{H}])$ is the value of equation (1) for Fe I, and $\delta([X/Fe])_{\text{model}}$ is the total error due to stellar parameters uncertainties (last column of Table 8). The total errors for abundances derived from EW are given in Tables 4-6 together with the abundance estimates. For the error bars reported in all our abundance plots (always shown in the lower left corner of Figs. 8-12) we have adopted two error sources. The first due to stellar parameters uncertainties (leftmost side of the plots) comes directly from Table 8, whereas the second (more to the right side) represents the error associated with the abundance analysis - for those derived from the EW, this is the mean error of Tables 4,5, and 6, and for those elements with abundances derived from spectrum synthesis, it is the value described earlier on in this Section.

5. Abundance Distributions and comparison to Galactic samples

In Figs. 8 to 12 we depict the chemical distributions for the α -elements, the iron-peak group, Na, Sc, Cu and s -elements for our stars compared to different samples of the Galaxy. Our data are represented as blue dots and the MW disk and halo data are depicted by black symbols. The references of the disk are: Fulbright 2000 (crosses); Reddy et al. 2003 (open squares); Allende Prieto et al. 2004 (open stars); Bai et al. 2004 (open circles); Prochaska et al. 2000 (open triangles); Burris et al. 2000 (stars - only for the

heavy-elements plots); Johnson & Bolte 2002 (open triangles - only for the heavy-elements plots); Simmerer et al. 2004 (open hexagons); Nissen & Shuster 1997 (cyan asterix, only stars with low $[\alpha/\text{Fe}]$ ratios); Nissen et al. 2000 (cyan asterix - Sc abundances for the low- α stars); and Bensby et al. 2004 (open squares - only for the oxygen plot). LMC globular clusters (GC) samples of Hill et al. (2000, hereafter HI00) for O, and Hill (2004 hereafter HI04) for Na, Mg, Ca and Si are plotted as green open down triangles; and of Johnson et al. 2004 for the α -elements Ca, Si and Ti are represented as open magenta triangles; field LMC red giants of Smith et al. (2002, hereafter SM02) are depicted as red open pentagons. Error bars as described in Sect.4.0.1 are shown in the lower left side of the plots.

5.1. Ca, Si and Ti

In Fig. 8, the chemical distributions for Ca, Si, and Ti I are depicted. We have found that $[\text{Si}/\text{Fe}]$ follows roughly the solar ratio with some scatter. $[\text{Ca}/\text{Fe}]$ shows a slight decrease with metallicity. Compared to the distribution of the galactic halo (GH), both silicon and calcium mean abundances are deficient by a factor of 3. Ti I ratios are also underabundant relative to galactic disk (GD) and GH samples, and agree very well with the results of SM02, who derived titanium abundances from neutral lines for a sample of red giants from LMC disk. There is a hint for a decreasing trend of Ti abundances for higher metallicity stars especially when SM02 datapoints are taken into account together with our sample. Compared to LMC GC of HI04, we have found that the two stars of our sample with metallicities similar to those of those of HI04 have also similar $[\text{Ca}/\text{Fe}]$ ratios. Johnson et al. (2004) sample of GC stars seems to overlap our $[\text{Ca}/\text{Fe}]$ and $[\text{Ti}/\text{Fe}]$ distributions, while their $[\text{Si}/\text{Fe}]$ ratios are enhanced.

A very interesting result from these plots emerge comparing our data with those of Nissen & Shuster 1997 (hereafter NS97, cyan squares). NS97 discovered a sample of stars from the galactic halo with abnormal abundances: low $[\alpha/\text{Fe}]$, $[\text{Na}/\text{Fe}]$ and $[\text{Ni}/\text{Fe}]$ ratios compared to "standard" halo stars. Such chemically peculiar or "low- α " halo stars have an important role in elucidating the possible merging history of the GH. Comparing the two distributions, we have found that NS97 stars show a slightly enhanced mean α abundance relative to our LMC stars.

Si, Ca and Ti are predicted to be produced in intermediate mass Type II SNe (SNe II) with a smaller contribution from Type Ia SNe (SNe Ia) (e.g. Tsujiomoto et al. 1995, Thielemann et al. 2002), while Fe is mostly produced by SNe Ia (e.g. Thielemann et al. 2001, Iwamoto et al. 1999). The low $[\alpha/\text{Fe}]$ ratios observed indicate that SNe Ia have contributed more to the ISM content in the past than the SNe II.

5.2. Mg, O, Na and Sc

In Fig. 9, abundance ratios are given for O, Mg, Sc and Na. Nucleosynthetic predictions attribute the main source of O, Mg and Na to high-mass stars, with $M > 25 M_{\odot}$, which explode as SNe II (Woosley & Weaver 1995, hereafter WW95), with Na production controlled by the neutron excess. Although WW95 have attributed the origin of Sc to SNe II, the main source of Sc production is still unclear (e.g. McWilliam 1997, Nissen et al. 2000).

As can be seen in the upper panel of Fig. 9, oxygen displays a slight underabundant behavior compared to GD and GH stars. For higher metallicities, it shows a faster decline with metallicity compared to stars from the galactic disk. From this figure we see that the different LMC samples agree very well, even the LMC globular clusters of Hill et al. (2000) and HI04. In the second plot we see that the [Mg/Fe] ratios for the LMC Inner Disk overlap those of the Galaxy, but with a smaller mean values. Na and Sc behaviors are similar to those of the α -elements Ti, and Si. Both elements are deficient and show smaller values for higher metallicities. It is important to notice that [Na/Fe] abundances in giants are still uncertain. Pasquini et al. (2004) found that [Na/Fe] ratios in giant stars are slightly higher than those from dwarf stars in the same cluster. High [Na/Fe] ratios were also inferred from giants in M67 (Tautvasiene et al. 2000). But such results have not been confirmed in the reanalysis of [Na/Fe] in giants and dwarfs of M67 (Randich et al. in press).

Nissen et al. (2000) also found that Sc behaves similarly to Na, showing lower [Sc/Fe] ratios for stars with lower $[\alpha/\text{Fe}]$, suggesting a correlation among those elements. In order to test the hypothesis of a correlation among Na and α -elements, and Sc and α -elements we have applied a statistical test to check for the existence and significance of such correlation. We have found that the correlations are weak: for Na-Ca, a correlation coefficient ϕ of 0.22 is found, and for Sc-Ca, $\phi = 0.40$. Few stars in the NS00 sample of "low- α " stars show small [Sc/Fe] ratios and overlap our sample, but most of them show solar [Sc/Fe] values, higher than in our LMC sample. Sodium abundances in NS97 sample are similar to our values, although with a higher mean abundance.

5.3. Iron-peak elements

Abundance distributions for the iron-peak elements are shown in Fig. 10. The iron-peak elements Co, Ni and Cr display a very distinct pattern in the LMC Inner Disk stars, never seen before in other stellar systems, with underabundant values compared to the Galactic distributions and many subsolar ratios. $[\text{Co}/\text{Fe}]$, $[\text{Cr}/\text{Fe}]$ and $[\text{Ni}/\text{Fe}]$ show a flat trend for most of the metallicity range, with mean abundances of ~ -0.25 dex for Cr and Ni, and ~ -0.20 dex for Co. $[\text{Co}/\text{Fe}]$ and $[\text{Cr}/\text{Fe}]$ indicate a possible increase for stars in the metal-poor tail.

The $[\text{V}/\text{Fe}]$ ratios are similar to the GD and GH patterns and track the solar value. NS97 low- α stars overlap our sample for Ni and Cr, but lie in the high abundance envelope of the distributions.

According to nucleosynthetic predictions, iron-peak elements are mainly produced in SNe Ia (Iwamoto 1999, Travaglio et al. 2005). While SNe Ia produce only $\approx 0.8 M_{\odot}$ of the solar iron-peak elements, SNe II produce $\approx 0.1 M_{\odot}$ (Timmes et al. 2003). The difference in the distributions from one environment to the other are an evidence that the production factors for each iron-peak element are not the same in the different types of SNe and depend on the SFH of the parent population. This will be further discussed in Sect. 7.

5.4. Copper

In Fig. 11 we show the plot for Cu. We have found that in the Inner Disk LMC stars, the copper distribution is flat, with a mean value of $[\text{Cu}/\text{Fe}] = -0.68$ dex. Comparing with the Galaxy, while in the metal-poor tail ($[\text{Fe}/\text{H}] < -1.3$ dex) there is an overlap between the two samples (LMC and Halo stars); for the higher metallicity range, the distributions diverge, with LMC stars showing a clear underabundance with respect to the Galactic Disk.

Although originally associated to the iron-peak elements, copper has still a very debated origin (e.g. Bisterzo et al. 2004, Cunha et al. 2004, Mishenina et al. 2002). Sometimes its main source is attributed to SNe Ia (Matteucci et al. 1993, Cunha et al. 2002, Mishenina et al. 2002) and sometimes to SNe II, particularly to a metallicity dependent mechanism (Bisterzo et al. 2004; McWilliam & Smecker-Hane 2005). If the chemical behavior of the present sample, with low $[\alpha/\text{Fe}]$, low [iron-peak/Fe] ratios, is due to a higher contribution from SNe Ia, the overall low $[\text{Cu}/\text{Fe}]$ pattern indicates that such type of supernovae cannot be the main source of Cu production.

5.5. *s*-process elements

We have found interesting chemical distributions for the *s*-process elements for our sample stars (Fig. 12). While the light-*s* elements, Zr and Y, present subsolar ratios with mean abundances of $[Y/Fe] = -0.31$ dex and $[Zr/Fe] = -0.52$ dex, with Zr showing a possible decreasing trend for increasing metallicities, the heavy-*s* elements La and Ba show supersolar values with enhanced pattern compared to those of the Galaxy. Ba has a peculiar behavior with high values for the metal-poor stars ($[Fe/H] < -1.4$ dex), a decreasing trend until $[Fe/H] = -1.15$ dex, and larger abundances for higher metallicity stars. La shows no trend with metallicity. One star, RGB_1118, has a particularly high La and Ba abundances ($[Ba/Fe]$ and $[La/Fe] \geq +1.0$ dex) and could be an *s*-enriched star (via mass-transfer from a former AGB companion), although it is not possible from our present data to discriminate between *s*- and *r*-enhancement. Comparing NS97 low- α stars with our sample, we find that these stars show abundance values nearer those of normal disk stars for Ba and Y than the LMC stars. The *hs/l*s ratios are high, with a mean value of $[hs/l] = +0.79$ dex, as can be seen in Fig. 13 (for consistency, in this picture we have derived the Ba and La ratios relative to Fe2). This is very different from what is observed for the GH and GD stars, which is around -0.2 to +0.2 dex (e.g. Pagel & Tautvaišienė 1997; Travaglio et al. 2004).

High abundances of elements heavier than Zr were also derived for LMC and SMC supergiants (Russell & Bessell 1989; Spite et al. 1993; Hill et al. 1995). Hill et al. (1995) for example, found that the light *s*-elements Zr and Y show solar composition in LMC supergiants while heavier *s*-elements (Ba, La, Nd) as well as the *r*-process element Eu are enhanced by +0.30 dex. As discussed by these authors, the overabundance of the heavier *s* and *r*-process elements seems to be a characteristic of the Magellanic Clouds, and indicate a particular evolution of that galactic system, although no satisfactory explanation was proposed for it.

In order to evaluate the *r* and *s* process contributions within our sample we analysed the *r*-process content of two of our sample stars for which we have UVES spectra that cover the Eu λ 6645 Å line. Eu and Ba abundances were derived for these spectra, in the same way we did for GIRAFFE spectra. For RGB_666 and RGB_808, we find respectively $[Ba/Fe] = 0.52$ and 0.24 dex, and europium abundances of $[Eu/Fe] = 0.40$ dex for RGB_666, and $[Eu/Fe] = 0.45$ dex for RGB_808. The corresponding $[Ba/Eu]$ ratios of 0.12 and -0.21 dex (to be compared with the solar *r*-process $[Ba/Eu] = -0.55$ and the solar *s*-process $[Ba/Fe] = +1.55$, following Arlandini et al. 1999), indicate that these stars contain a significant *r*-process contribution at low metallicity (RGB_808: $[Fe/H] = -1.65$) and a value close to the solar *s/r* mix at intermediate metallicities (RGB_666: $[Fe/H] = -1.10$).

A high r content seems to be in contradiction with the observed low $[\alpha/\text{Fe}]$ ratios (both being produced in massive stars). More data on Eu abundances are needed to confirm this high r content, and in particular, the trend of the s/r fraction (traced by $[\text{Ba}/\text{Eu}]$) as a function of metallicity will help to constrain the source of the high content of heavy s -elements in the LMC disk. We intend to tackle this issue in the two other fields (Bar and Outer Disk) of our LMC program, since one of the MEDUSA wavelength ranges covers the Eu line for these fields.

5.5.1. The NaMg, NaNi relations

In the paper by NS97 the authors have found a correlation between Na and Ni for their halo stars (both "normal" and "low- α " stars). Such correlation has been confirmed for a group of stars in the Dwarf Spheroidal Galaxies (Shetrone et al. 2003, SH03, Tolstoy et al. 2003, TO03, Venn et al. 2004). To evaluate this trend, we plot in Fig. 14 the $[\text{Ni}/\text{Fe}]$ vs. $[\text{Na}/\text{Fe}]$ relation for our sample stars (dots) together with NS97 low- α stars. We see that the LMC stars also show a correlation between Na and Ni, although with a flatter pattern than the increasing trend observed for the NS97 sample. According to Tsujimoto et al. (1995), Ni can be produced in SNe Ia without Na production; therefore, a higher contribution from SNe Ia would flatten the NaNi relation² (Venn et al. 2004) and could explain the behavior of the LMC stars. In Fig. 14 we also analyze the correlation between Na and Mg and we find decreasing $[\text{Na}/\text{Mg}]$ ratios for increasing $[\text{Mg}/\text{H}]$ ratios. The NS97 low- α stars seem a continuation of the observed trend.

6. Comparison to the Dwarf Spheroidal Galaxies

In Figs. 15 to 18 we compare the chemical distributions of our LMC sample to those of the dSph galaxies of Shetrone et al. (2003) and Tolstoy et al. (2003), and the Sagittarius dwarf galaxy (Sgr) of Bonifacio et al. (2004). Unfortunately the chemical distribution of most dSph galaxies is more concentrated in the metallicity range for which we have the lowest number of stars: $[\text{Fe}/\text{H}] < -1.2$, so the present analysis is not ideal. In Figs. 15 to 18 the distributions for the α -elements, Na, Sc and Cu and for the iron-peak elements are given (the description of the different symbols are given in the figure captions). As can be seen from these figures, there is an overlap among the LMC abundance ratios and those of the dSph galaxies for the α -elements, Sc and Na. Some of the stars from the Sgr dwarf galaxy overlap our sample for O, Ca and Si, but their $[\text{Mg}/\text{Fe}]$ ratios seem slightly deficient. $[\text{Cu}/\text{Fe}]$ ratios are also compatible with those found in dSph galaxies (with the exception of Fornax, which shows higher values for Cu). The iron-peak elements Cr, Co and Ni in the LMC sample show slightly smaller ratios than the dSph stars.

² however Travaglio et al. 2005 found that some Na and Mg are also produced in SNe Ia

For the s -process elements, the dSph galaxies also show enhanced hs and deficient ls compared to the Galactic behavior, although the general pattern is less discrepant than that showed by the LMC inner disk stars. Fornax has a more metal-rich star (Fnx21) with high s content, which may be an s -enriched star. The $[\text{Ba}/\text{Y}]$ ratios show a large offset relative to galactic samples, of the same order magnitude we have found. Venn et al. (2004) attribute such offset to primary s -process production by low-metallicity AGB stars.

7. Discussion

It is an amazing opportunity to have such numerous data about the chemical compositions of stars in an external galaxy. With this unique data-set, we can now explore in more detail the SFH and better understand better the evolution of the LMC disk. The overall low $[\text{X}/\text{Fe}]$ ratios indicate that such stars have undergone a global process which is different from that experienced by the average halo and disk stars in the Galaxy. In this section we discuss the possible explanations for such behavior.

As seen in previous sections, small $[\alpha/\text{Fe}]$ ratios have been already observed in other stellar systems such as the chemically peculiar halo stars (NS97, NS00), the dSph galaxies of the Local Group (Shetrone 2003, Tolstoy 2003), and the Sagittarius dSph galaxy (Smecker-Hane & McWilliam 2002, Bonifacio et al. 2004). It is interesting to notice that the s -process trends in the dSph galaxies (enhanced hs and deficient ls ratios) are the same as for our stars. Correlations between abundances of iron-peak elements and α -elements are not completely unknown, although observed in a much less evident magnitude in other stellar systems. A slight deficient pattern for Ni and Cr has been observed for the low- α stars of NS97. Bensby et al. (2003) also found a correlation among the $[\text{iron-peak}/\text{Fe}]$ and $[\text{Na}/\text{Fe}]$ vs. $[\alpha\text{-elements}/\text{Fe}]$ abundance ratios, i.e., slightly higher $[\text{Cr}/\text{Fe}]$, $[\text{Ni}/\text{Fe}]$ and $[\text{Na}/\text{Fe}]$ ratios in thick disk with enhanced $[\alpha\text{-element}/\text{Fe}]$ ratios (see their Fig. 13).

Many interpretations have been given for the small $[\alpha/\text{Fe}]$ ratios observed. One hypothesis is that the star formation (SF) developed slowly, in short bursts, followed by long quiescent periods without SF, during which the SNe Ia contaminated the ISM increasing the Fe content (e.g. Gilmore & Wyse 1991). Smaller SNe II/SNe Ia ratios, therefore a higher frequency of SNe Ia relative to SNe II, have also been invoked, within a bursty or continuous regime, and with or without galactic winds (e.g. Pagel & Tautvaišienė, 1997, Smith et al. 2002); a steepened IMF relative to that of the solar neighborhood has been proposed by Tsujimoto et al. (1995) and de Freitas Pacheco (1998), whereas alpha-enriched galactic winds, which would lower the $[\alpha/\text{Fe}]$ content, have been suggested by Pilyugin (1996).; and finally a small (low-mass) star-formation event, which would effectively truncate the IMF, yielding fewer high-mass SNe II than for normal SF

events (Tolstoy et al. 2003). To find explanations for the behavior of the iron-peak elements is more puzzling, since they are predicted to be basically produced in SNe Ia (e.g. Travaglio et al. 2005). A possible explanation is that the yields of the SNe Ia are metallicity dependent (Timmes et al. 2003).

The abundance distributions observed for the *hs* and the *ls* elements, with $hs/ls=[Ba+La/Y+Zr]$, are in agreement with the hypothesis that *s*-process elements production in AGB stars is metallicity dependent (Busso et al. 1999 and references therein; Busso et al. 2001; Abia et al. 2003, Travaglio et al. 2004). It has been noticed that, due to details on the nucleosynthesis of the *s*-process, *hs*-elements (e.g. Ba, La and Nd) are preferentially produced by metal-poor AGB stars compared to *ls* elements (e.g. Y, Zr and Sr), which have instead their production peak at $[Fe/H] \approx -0.1$ (e.g. Fig. 1 of Travaglio et al. 2004). If the SF is slow, low-metallicity AGB stars have enough time to contaminate the ISM, leaving noticeable chemical signatures for the next generations.

Nevertheless, Venn et al. (2004) discuss if the abundances of the dSph galaxies of such elements are indeed due to the *s*-process or if they have a strong contribution from the *r*-process, including Y. Also, according to Richtler et al. (1989) and Russell & Dopita (1992), the most probable explanation for the high Ba and La abundances observed in the Magellanic Clouds is an additional *r*-process component. This would mean that *hs* and *ls* elements are produced in different rates by the *r*-process nucleosynthesis, probably in different sites. Therefore, the analysis of the behavior of the *s*-elements in the given metallicity range is complex and must take into account both the *r* and the *s* contributions.

7.1. Galaxy Formation and Evolution

One of the most debated themes about galaxy formation in the Universe within a Λ CDM hierarchical scenario concerns the problem of overprediction of the number of galaxies at low-*z* and underprediction at high-*z* (Cimatti et al. 2002). One of the consequences for the Local Group is a larger number of small galaxies than is actually observed. According to these models, numerous merging and accretion events play an important role in the formation process of massive galaxies (e.g. Moore et al. 1999). The quest for signatures of possible accreted stars from nearby galaxies in the Galactic halo and disk have been carried out, without definite conclusions (NS97, NS00, Ivans et al. 2003, Venn et al. 2004). A careful inspection on the chemical distributions of the different Galactic components, with the low dispersion in the abundance ratios at each metallicity bin, and the smooth transitions between them (see e.g. plots from Venn et al. 2004), seem to indicate a different process: that the whole Galaxy has been built within a global process, rather than by many accreting events, even for the galactic halo (see Gilmore & Wyse 2004). Such observational features hint for a common history within the same environment

rather than a mix of SFHs. The results from the present work strongly support this idea. As one of the nearest satellites of the MW, with a long kinematic interactional history with our galaxy, the LMC is an obvious target for searching for possible interacting signatures. We have found that the chemical compositions of the LMC Inner Disk stars show a different pattern when compared to their galactic counterparts (if we exclude the low- α stars of NS97). This indicates that possible major merging events with this galaxy are unlikely, but strong conclusions are not possible because we need a more representative sample. The chemical distributions of the LMC Inner Disk also hint for a different process of galaxy formation, showing that the galactic local environment is fundamental for the chemical evolution of its components.

8. Summary

In the present paper we report abundance ratios for a series of elements, including α , s and iron-peak elements, Na, Sc and Cu for a sample of stars (62) of the inner disk of the LMC. We have found a very different behavior for most of the elements relative to stars from the Galaxy with similar metallicity, hinting at a very different evolutionary history. The main results are summarized as follows:

- $[\alpha/\text{Fe}]$ ratios show an overall deficient pattern relative to Galactic distributions
- the $[\text{X}/\text{Fe}]$ deficiency of the α -elements is also followed by Na, Sc, Cu and, in an unexpected behavior, by the iron-peak elements Ni, Cr and Co
- we have found relationships between NaNi and NaMg , in agreement to those derived by Nissen & Schuster (1997) for their low- α halo stars
- Cu abundance ratios show very small values, $[\text{Cu}/\text{Fe}] \simeq -0.60$ dex, with no apparent trend with metallicity.
- s -process elements behavior is dichotomic: while high- s elements (Ba and La) present an enhanced pattern, low- s elements (Y and Zr) are deficient relative to the galactic samples. Such behavior has been observed before in LMC and SMC F supergiants and in the dSph galaxies stars.
- we have derived Eu abundances for two of our stars, and found $[\text{Eu}/\text{Fe}] = +0.40$ dex. Eu abundances are important for the elucidation of r/s contributions and the chemical history of the population. For the next two fields (see Introduction) the wavelength range of the spectra covers this line and a better evaluation of such contributions will be possible.
- compared to the dSph galaxies we have found similar abundance ratios for almost all the elements, with a mild deficiency of Cr and Ni, and slight enhancements of La, Ba, Na and Y. LMC Inner Disk abundances of Ca, Si, O and Mg are also similar to those of the Sagittarius dwarf galaxy.

- the alike pattern between the LMC inner disk population and the samples of the dSph galaxies indicate that all these galaxies may have undergone similar SFH
- the low- α stars of NS97 have abundance trends similar to ours for most elements (if one excludes the heavy s elements). From the chemical point of view, an accreting origin from the LMC for those stars cannot be totally excluded.

Acknowledgements. L. P. acknowledges CAPES and FAPESP fellowships #0606-03-0 and #01/14594-2. We greatly thank Peter Stetson for the availability of the DAOSPEC program.

References

- Abia, C., Domguez, I., Gallino, R., Busso, M., Masera, S., Straniero, O., de Laverny, P., Plez, B., Isern, J. 2002, ApJ 579, 817
- Allende Prieto, C., Barklem, P. S., Lambert, D. L., Cunha, K. A&A 420, 183
- Bai, G. S., Zhao, G., Chen, Y. Q., Shi, J. R., Klochkova, V. G., Panchuk, V. E., Qiu, H. M., Zhang, H. W. 2004, 2004, A&A 425, 671
- Bensby, T., Feltzing, S., Lundstrom, I. 2003, A&A 410, 527
- Bensby, T., Feltzing, S., Lundstrom, I. 2004, A&A 415, 155
- Bessell, M.S., Castelli, F. & Plez, B. 1998, A&A 333, 231
- Bessell, M.S. 1991, A&A 242L, 17
- Biehl, D. 1976, Ph.D. Thesis, Kiel
- Bisterzo, S., Gallino, R., Pignatari, M., Pompeia, L., Cunha, K., Smith, V. 2004, MmSAI v.75, p.741
- Bonifacio, P., Sbordone, L., Marconi, L., Pasquini, L., Hill, V. 2004, A&A 414, 503
- Bord, D. J., Barisc Bisterzo, S., Gallino, R., Pignatari, M., Pompeia, L., Cunha, K., Smith, V., Iano, L. P., & Cowley, C. R. 1996, MNRAS, 278, 997
- Burris, D.L., Pilachowski, C.A., Armandroff, T.E., Sneden, C., Cowan, J.J., Roe, H. 2000, ApJ 544, 302
- Busso, M., Gallino, R., & Wasserburg, G. J. 1999, ARA&A, 37, 239
- Busso, M., Gallino, R., Lambert, D.L., Travaglio, C., Smith, V.V. 2001, ApJ 557, 802
- Carpenter, J.M. 2001, AJ, 121, 2851
- Cayrel, R. 1988, in in IAU Symp. 132, The Impact of Very High S/N Spectroscopy on Stellar Physics, ed. G. Cayrel de Strobel & M. Spite (Dordrecht: Kluwer), 345
- Cimatti, A., Pozzetti, L., Mignoli, M., Daddi, E., Menci, N., Poli, F., Fontana, A., Renzini, A., Zamorani, G., Broadhurst, T., Cristiani, S., D’Odorico, S., Giallongo, E., Gilmozzi, R. 2002 A&A 391L, 1
- Cayrel, R., Depagne, E., Spite, M., Hill, V., Spite, F., Francois, P., Plez, B., Beers, T., Primas, F., Andersen, J., Barbuy, B., Bonifacio, P., Molaro, P., Nordström, B. 2004, A&A 416, 1117
- Cunha, K., Smith, V.V., Suntzeff, N.B., Norris, J.E., Da Costa, G.S., Plez, B. 2004, AJ 124, 379
- D’Onghia, E., & Lake, G., 2004 ApJ 612 628
- de Freitas Pacheco, J.A. 1998, Aj 116, 1701
- de Vaucouleurs, G. 1980, PASP 92, 576

- Edvardsson, B. Andersen, J., Gustafsson, B., Lambert, D. L., Nissen, P. E., Tomkin, J. 1993, *A&A* 275, 101
- Fernie, J.D. 1983, *PASP* 95, 782
- Fulbright, J. P. 2000, *AJ* 120 1841
- Gilmore G., Wyse R.F.G. 1991, *ApJ* 367, L55
- Gilmore G., Wyse R.F.G. 2004, astro-ph/0411714
- Grevesse, N., Sauval, A. J. 2000, in "Origin of Elements in the Solar System, Implications of Post-1957 Observations, Proc". of the International Symposium. Edited by O. Manuel. Boston/Dordrecht: Kluwer Academic/Plenum Publishers, p.261
- Hill, V., Andrievsky, S. Spite, M. 1995, *A&A* 293, 347
- Hill, V., Francois, P., Spite, M., Primas, F., & Spite, F. 2000, *A&A* 364 L19
- Hill, V. 2004, in *Carnegie Observatories Astrophysics Series, Vol. 4: Origin and Evolution of the Elements*, ed. A. McWilliam and M. Rauch (Cambridge: Cambridge Univ. Press), p.205
- Ivans, I.I., Sneden, C., James, C.R., Preston, G.W., Fulbright, J.P., Hflich, P.A., Carney, B.W., Wheeler, J.C. 2003, *ApJ* 592, 906
- Iwamoto, K., Brachwitz, F., Nomoto, K., Kishimoto, N., Umeda, H., Hix, W.R., Thielemann, F.-K. 1999, *ApJS* 125, 439
- Johnson, J. & Bolte, M. 2002, *ApJ* 579, 616
- Johnson, J., Bolte, M., Hesser, J.E., Ivans, I.I. 2004, in *Carnegie Observatories Astrophysics Series, Vol. 4: Origin and Evolution of the Elements*, ed. A. McWilliam and M. Rauch, p. 29
- Kraft, R.P. Sneden, C., Langer, G.E. & Prosser, C.F. 1992, *AJ* 104, 645
- Kurucz, R.L., Furenlid, I., Brault, J. 1984, *National Solar Observatory Atlas, Sunspot, New Mexico: National Solar Observatory*, 1, 984
- Lawler, J. E., Bonvallet, G., Sneden, C. 2001, *ApJ* 556, 452
- Luck, R.E. & Lambert, D.L. 1992, *ApJS* 79, 303
- Matteucci, F., Raiteri, C.M., Busson, M., Gallino, R., & Gratton, R. 1993, *A&A*, 272, 421
- McWilliam, A. 1997, *ARA&A* 35, 503
- McWilliam, A. 1998, *AJ* 115, 1640
- McWilliam, A., Smecker-Hane, T. 2005, *ApJ* 622, 29
- Mishenina, T. V., Kovtyukh, V. V., Soubiran, C., Travaglio, C., & Busso, M. 2002, *A&A*, 396, 189
- Moore, B., Ghigna, S., Lake, G., Quinn, T., Stadel, J., & Tozzi, P. 1999, *ApJ*, 524, L19
- Nissen, P. E., Schuster, W. J. 1997, *A&A* 326, 752
- Nissen, P. E., Chen, Y. Q., Schuster, W. J., Zhao, G., 2000, *A&A* 353, 722
- Pagel, B. E. J., Tautvaišiene, G. 1997, *MNRAS* 288, 108
- Pasquini, L., Avila, G., Blecha, A. et al. 2002, *The Messenger*, 110, 1
- Pasquini, L., Randich, S., Zoccali, M., Hill, V., Charbonnel, C., Nordström, B. 2004, *A&A* 424, 951
- Pilyugin, L.S. 1996, *A&A* 310, 751
- Plez, B., Brett, J.M., Nordlund, A. 1992, *A&A* 256, 551
- Plez, B. 2000, *Proc. IAU Symp.* 177, 'The Carbon Star Phenomenon', Wing, R.F. ed., Kluwer Academic Publishers, Dordrecht, p.71

- Prochaska, J. X., Naumov, S. O., Carney, B. W., McWilliam, A., & Wolfe, A. M. 2000, *AJ* 120 2513
- Reddy, B. E., Tomkin, J., Lambert, D. L., & Allende Prieto, C. 2003, *MNRAS* 340, 304
- Richtler, T., Spite, M., Spite, F. 1989, *A&A* 225, 351
- Russell, S.C. & Bessell, M.S. 1989, *ApJS* 70, 865
- Russell, S.C. & Dopita, M.A. 1992, *ApJ* 384, 508
- Rutten, R.J., 1978, *Solar Physics* 56, 237
- Shetrone, M. D., Venn, K. A., Tolstoy, E., Primas, F., Hill, V., & Kaufer, A. 2003, *AJ*, 125, 684
- Smecker-Hane, T.A., Cole, A.A., Gallagher, J.S.III, Stetson, P.B. 2002, *SMH02*, *ApJ* 566, 239
- Smecker-Hane T., Cole A., Mandushev, G.I., Bosler, T. L., Gallagher J., in press
- Smecker-Hane T., McWilliam, A. 2002, *Proc. Symp. ‘Cosmic Abundances as Records of Stellar Evolution and Nucleosynthesis in honor of David L. Lambert’ ASP Conf. Series*, Thomas G. Barnes III and Frank N. Bash eds., San Francisco, V. 336, 221
- Smith, V.V., Hinkle, K.H., Cunha, K., Plez, B., Lambert, D.L., Pilachowski, C.A., Barbuy, B., Meldez, J., Balachandran, S., Bessell, M.S., Geisler, D.P., Hesser, J.E., Winge, C. 2002, *AJ* 124, 3241
- Snedden, C., Gratton, R.G., Crocker, D.A. 1991, *A&A*, 246, 354
- Spite, M. 1967, *Ann. d’Astrophys.*, 30, 21
- Spite, F., Barbuy, B., Spite, M. 1993, *A&A* 272, 116
- Tautvaiiene, G., Edvardsson, B., Tuominen, I., Ilyin, I. 2000, *A&A*, 360, 499
- Thielemann, F.-K., Brachwitz, F., Freiburghaus, C., Kolbe, E., Martinez-Pinedo, G., Rauscher, T., Rembges, F., Hix, W. R., Liebendrfel, M., Mezzacappa, A., Kratz, K.-L., Pfeiffer, B., Langanke, K., Nomoto, K., Rosswog, S., Schatz, H., Wiescher, W. 2001, *PPNP*, 46, 5
- Thielemann, F.-K., Argast, D., Brachwitz, F., Martinez-Pinedo, G., Rauscher, T., Liebendrfel, M., Mezzacappa, A., Hflich, P., Nomoto, K. 2002, *Ap&SS* 281, 25
- Timmes, F. X., Brown, Edward F., Truran, J. W. 2003, *ApJ* 590, 83L
- Tolstoy, E., Venn, K. A., Shetrone, M. D., Primas, F., Hill, V., Kaufer, A., & Szeifert, T. 2003, *AJ*, 125, 707
- Travaglio, C., Gallino, R., Arnone, E., Cowan, J., Jordan, F., Sneden, C. 2004, *ApJ* 601, 864
- Travaglio, C. Hillebrandt, W., Reinecke, M., Thielemann, F.-K, 2005, *astro-ph/0406281*
- Tsujimoto, T., Nomoto, K., Yoshii, Y., Hashimoto, M., Yanagida, S., Thielemann, F.-K. 1995, *MNRAS* 277, 945F
- Venn, K.A., Irwin, M., Shetrone, M.D., Tout, C.A., Hill, V., Tolstoy, E. 2004, *AJ* 128, 1177
- Westerlund, B. E. 1997, *The Magellanic Clouds Cambridge: Cambridge Univ. Press*)
- Woosley, S.E., Weaver, T.A. 1995, *ApJS* 101, 181

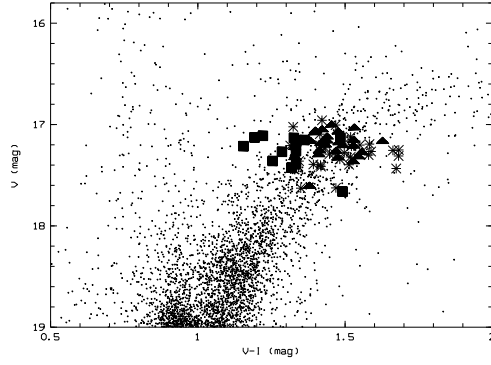


Fig. 1. V ($V-I$) color-magnitude diagram of the Disk region (following SH02), with our sample stars overplotted: *asterisks* are stars with $[\text{Fe}/\text{H}]_{\text{CaT}} \geq -0.5$ dex, *triangles* $-1.0 \leq [\text{Fe}/\text{H}]_{\text{CaT}} < -0.5$ dex, *squares* $[\text{Fe}/\text{H}]_{\text{CaT}} < -1.0$ dex.

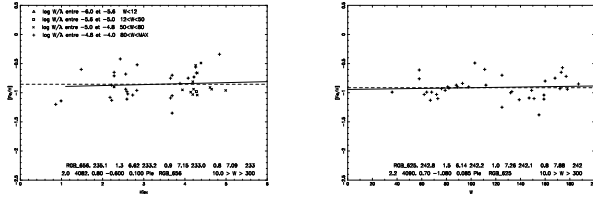


Fig. 2. Example of temperature and microturbulence velocity calculation: $[\text{Fe I}/\text{H}]$ vs. χ_{exc} (left panel) and $[\text{Fe I}/\text{H}]$ vs. EW (right panel) for RGB_625 (see text).

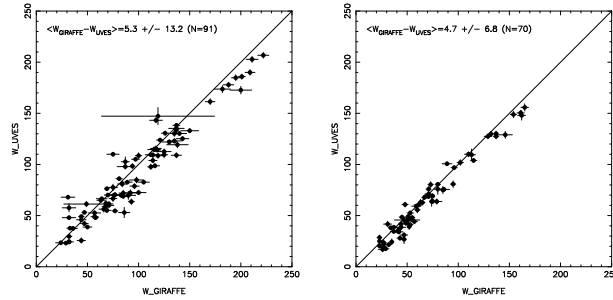


Fig. 3. Comparison between UVES and GIRAFFE spectra analyses. In the left plot the EWs of RGB_666 are given, and in the right plot, those for RGB_808.

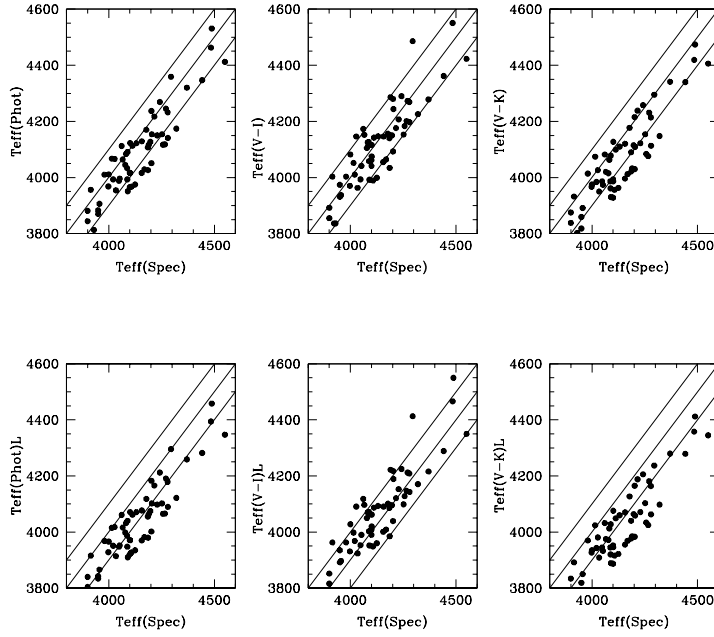


Fig. 4. Comparison between photometric and spectroscopic temperatures (see text). On the bottom plots, photometric temperatures are derived with $E(B-V)=0.03$ (SMH02), while on the upper plots, photometric temperatures are derived with a higher reddening value, $E(B-V)=0.06$ (Bessel 1991). Solid lines represent $T_{\text{eff}(\text{spec})} = T_{\text{eff}(\text{phot})}$ and $T_{\text{eff}(\text{spec})} = T_{\text{eff}(\text{phot})} \pm 100\text{K}$.

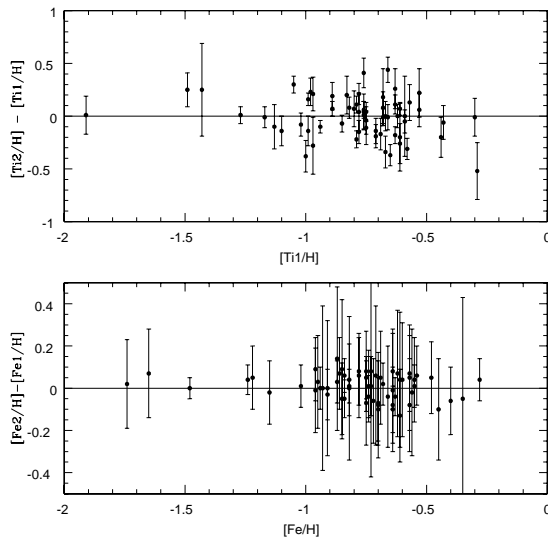


Fig. 5. Gravity check: difference between ionized and neutral species vs. neutral species (error bars are given for each point) for titanium and iron.

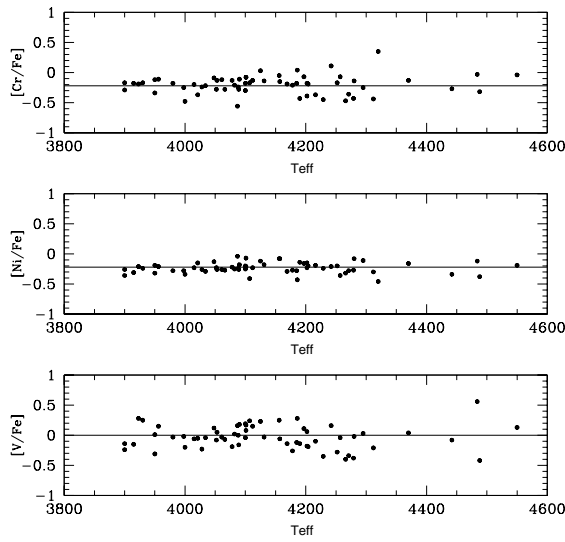


Fig. 6. Abundance ratios against temperatures. From top to bottom: $[\text{Cr}/\text{Fe}]$ vs. T_{eff} , $[\text{Ni}/\text{Fe}]$ vs. T_{eff} and $[\text{V}/\text{Fe}]$ vs. T_{eff} .

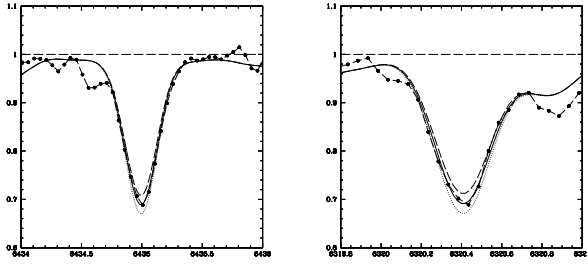


Fig. 7. Example of the line synthesis procedure for the Y I and La II lines: left panel: Y I $\lambda 6435\text{\AA}$ line fitting for RGB_752; right panel: La II $\lambda 6320$ line fitting for RGB_690. The black circles depict the observed spectra and the lines are the synthetic spectra. Abundances of the synthetic spectra are: $[\text{Y}/\text{Fe}] = -0.55$ (dashed line), -0.45 (continuous line - best fit), -0.25 (dotted line); and $[\text{La}/\text{Fe}] = 0.56$ (dashed line), 0.66 (continuous line - best fit), and 0.76 (dotted line).

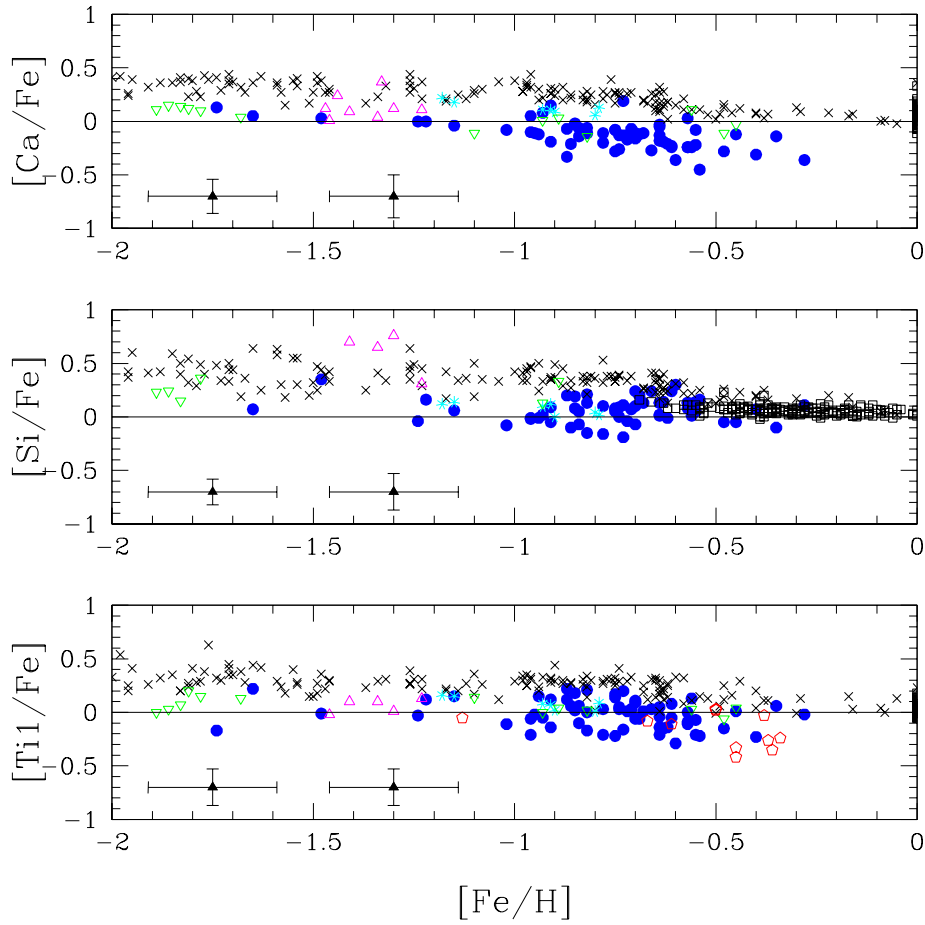


Fig. 8. Abundance distributions for the Inner Disk LMC stars: $[\alpha/\text{Fe}]$ vs. $[\text{Fe}/\text{H}]$ (blue dots). Galactic samples are represented with black symbols (see Sect. 5 for details). Cyan squares are the data for the low- α stars of NS97. The other colored filled symbols represent data from the LMC (see Sect. 5).

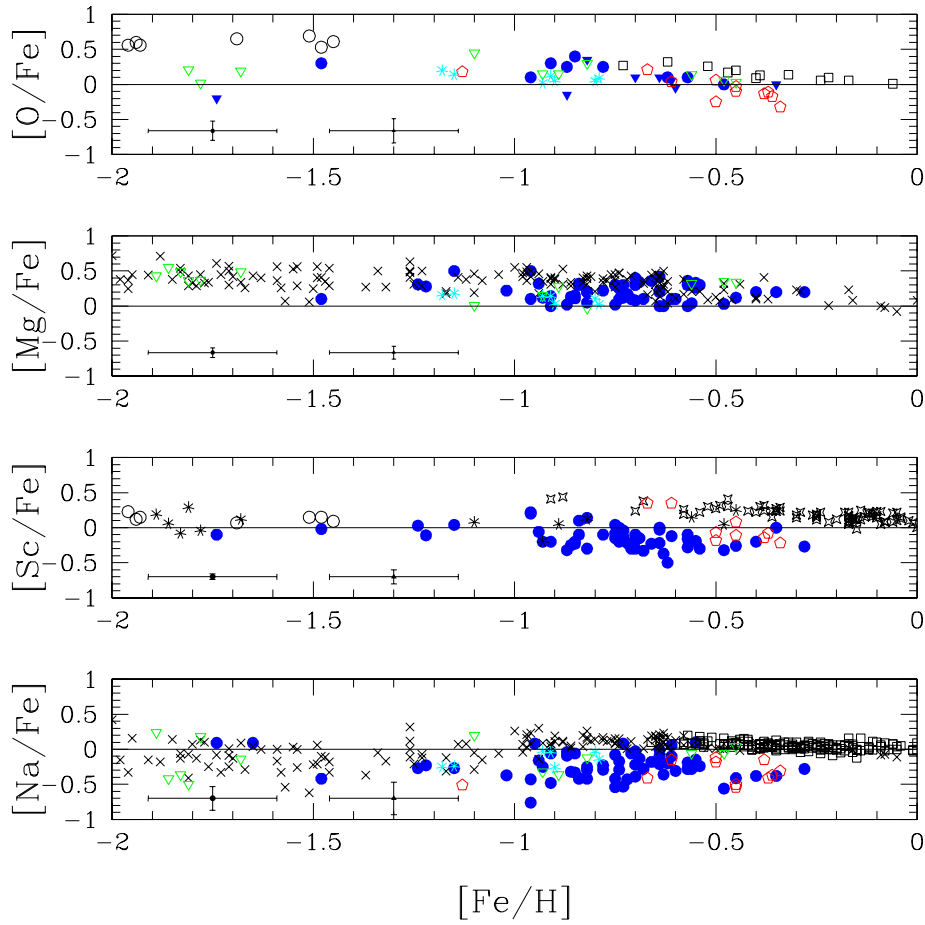


Fig. 9. Abundance distributions for the Inner Disk LMC stars: $[\text{O}, \text{Mg}, \text{Na}, \text{Sc}/\text{Fe}]$ vs. $[\text{Fe}/\text{H}]$ (symbols are the same as in Fig. 8).

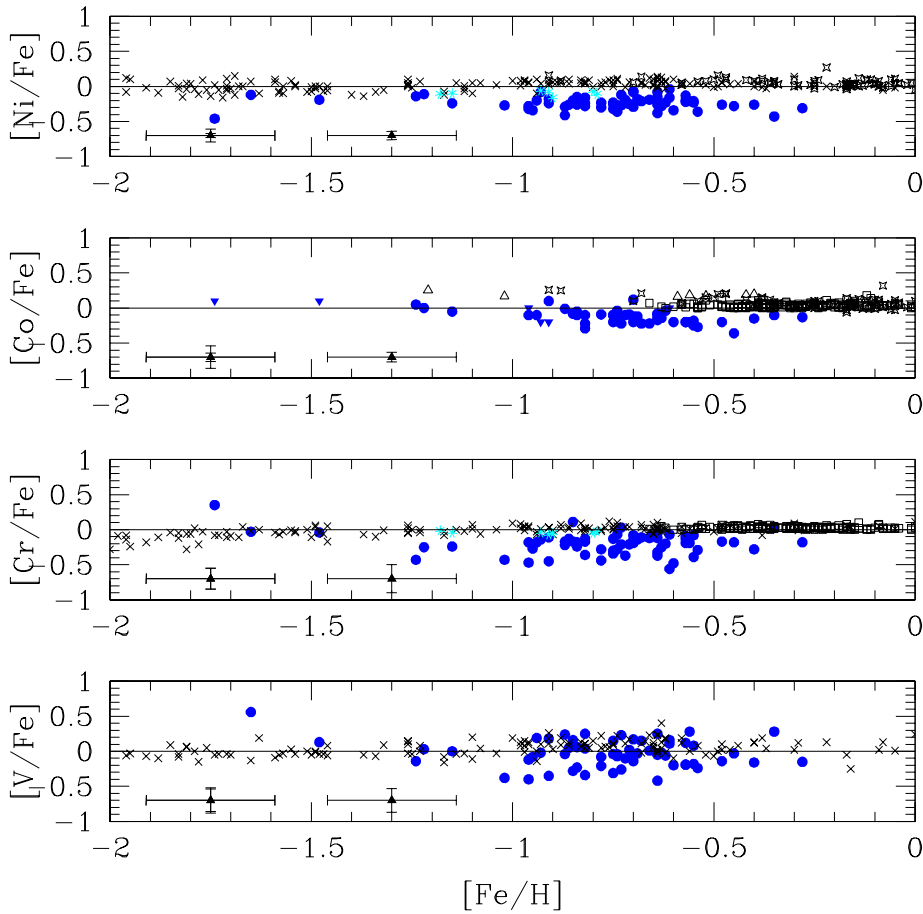


Fig. 10. Abundance distributions for the Inner Disk LMC stars: [Iron-peak/Fe] vs. [Fe/H] (symbols are the same as in Fig. 8).

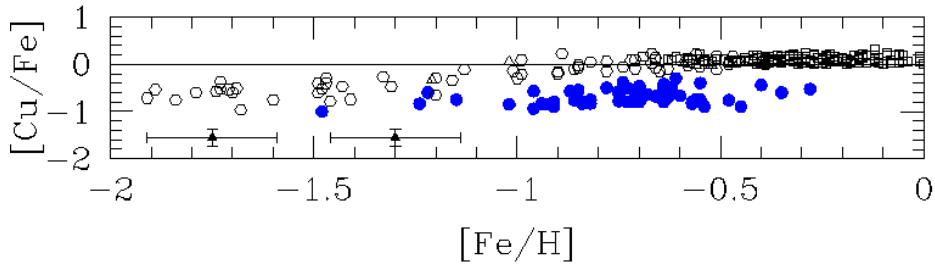


Fig. 11. Abundance distributions for Inner Disk LMC stars: Copper. The symbols are the data from: our sample stars (blue circles); Mishenina et al. 2002 (open hexagons); Prochaska et al. 2002 (open triangles); Reddy et al. 2003 (open squares).

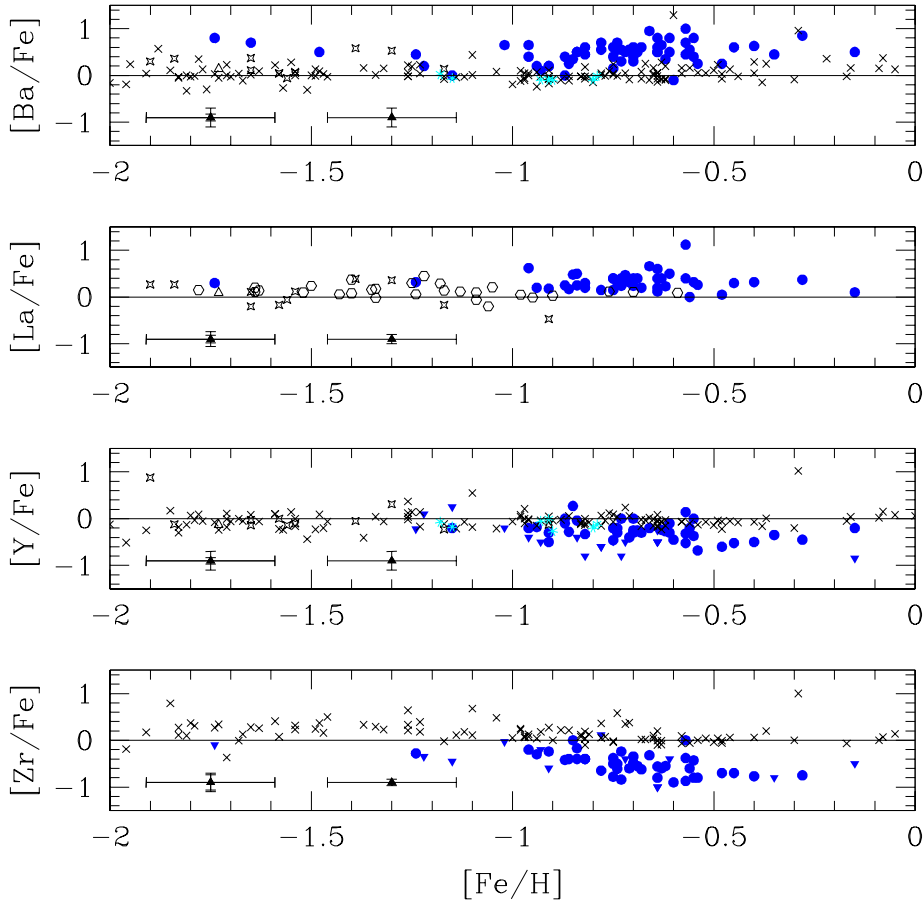


Fig. 12. Abundance distributions for Inner Disk LMC stars: $[s\text{-elements}/\text{Fe}]$ vs. $[\text{Fe}/\text{H}]$. Blue dots depict our sample stars and cyan asterisk, the low- α stars from NS97. Black symbols represent galactic samples (see Sect. 5 for details).

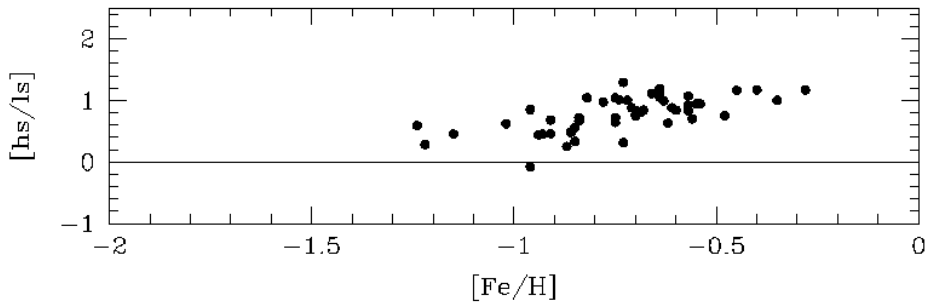


Fig. 13. Observed abundance ratios $[hs/ls] = [\text{Ba} + \text{La}/\text{Y} + \text{Zr}]$.

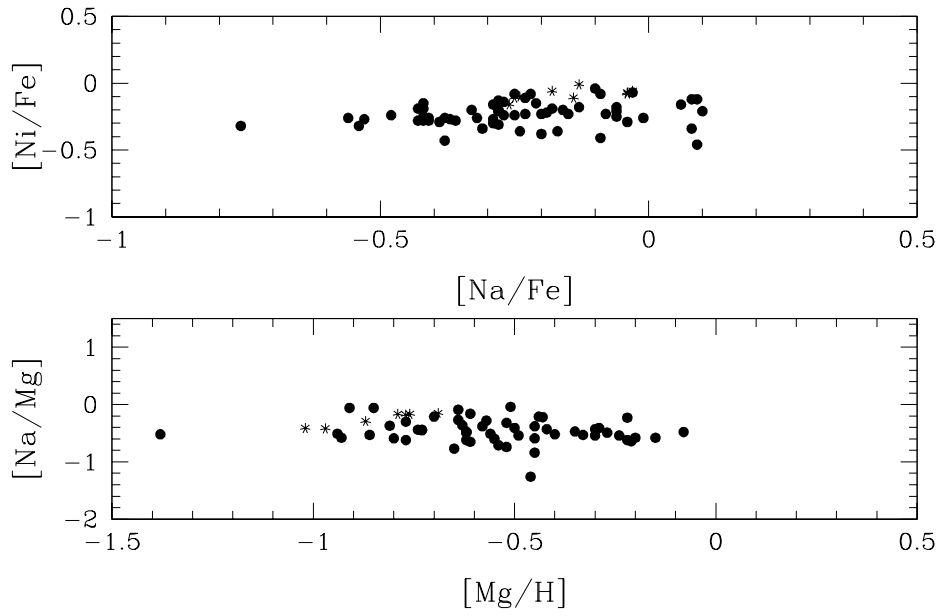


Fig. 14. The NaNi and NaMg abundance relations. Our sample stars are depicted as dots and NS97 low- α stars as starred symbols.

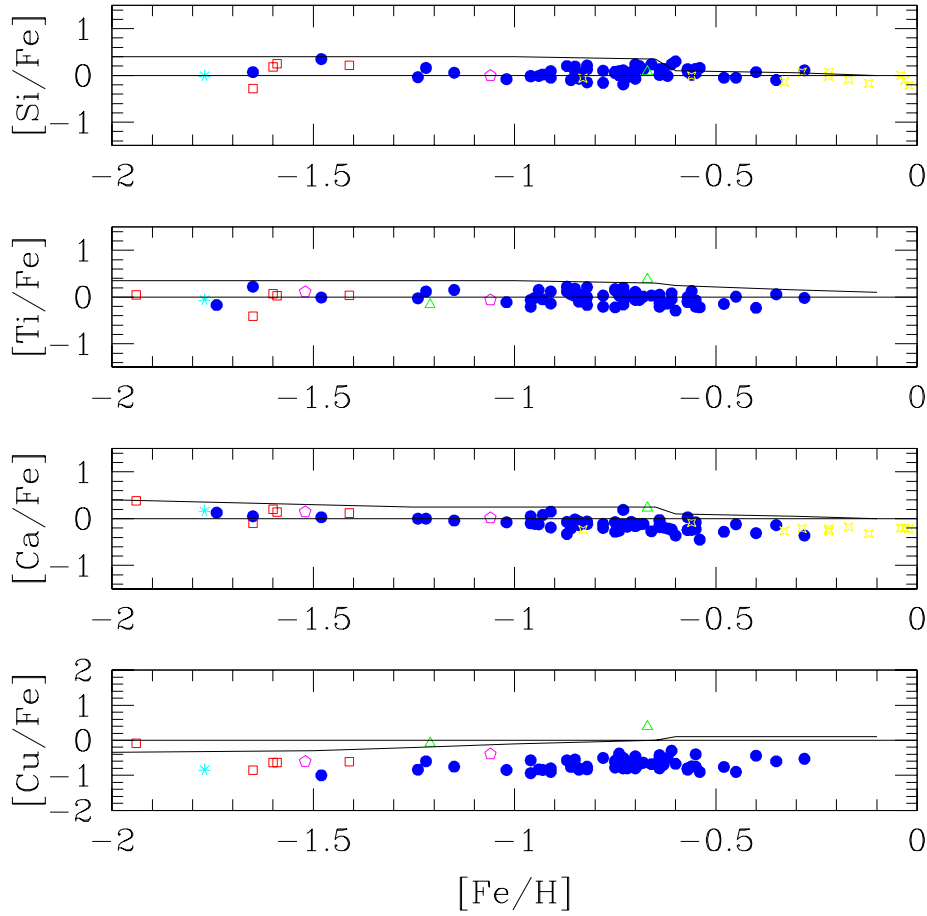


Fig. 15. Comparison of the Inner Disk LMC stars with stars from the dwarf spheroidal galaxies and the Sgr galaxy. 1. Alpha elements. The symbols are: our sample (blue dots), Leo I (magenta pentagons), Sculptor (cyan dots), Fornax (green triangles), Carina (red squares), and Sgr (yellow stars).

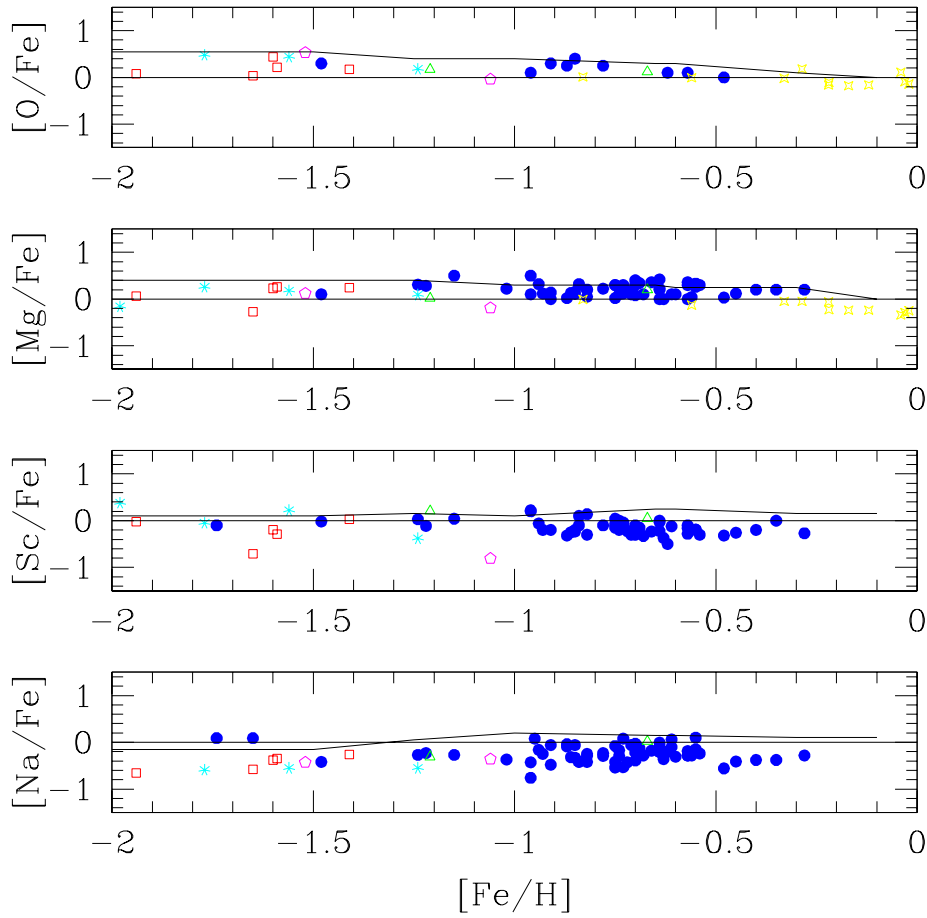


Fig. 16. Comparison of the Inner Disk LMC stars with stars from the dwarf spheroidal galaxies and the Sgr galaxy. 2. O, Mg, Na and Sc (symbols are the same as in Fig. 15).

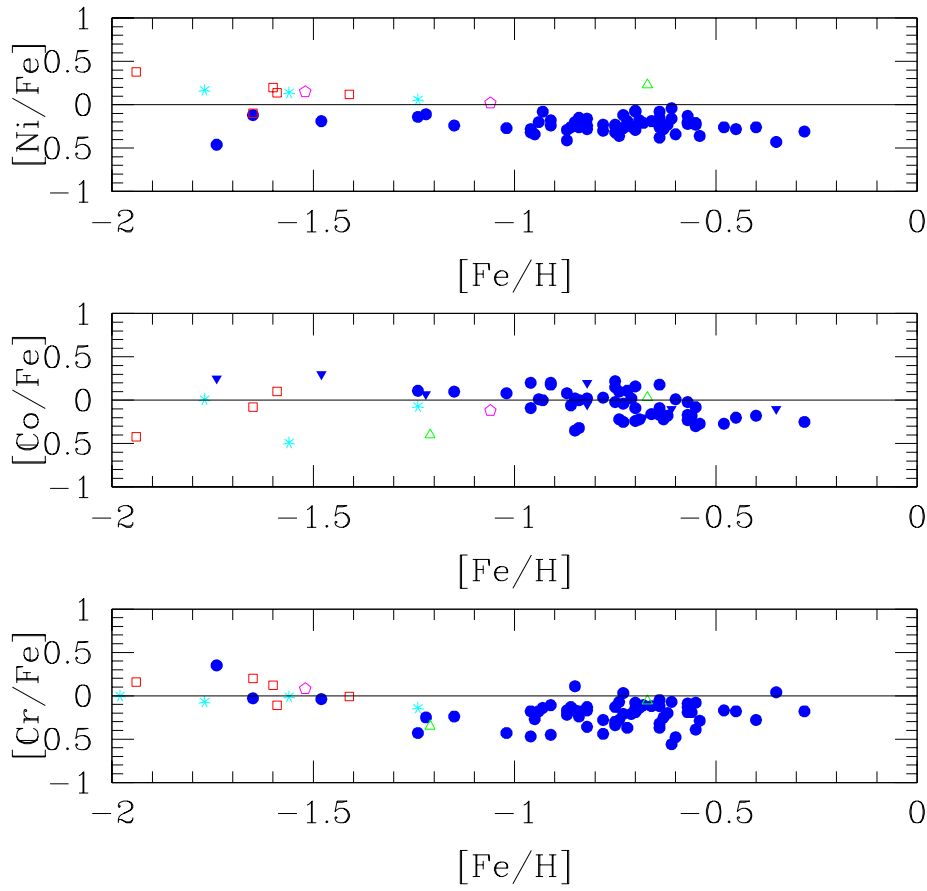


Fig. 17. Comparison of the Inner Disk LMC stars with stars from the dwarf spheroidal galaxies. 3. Iron-peak elements (symbols are the same as in Fig. 15).

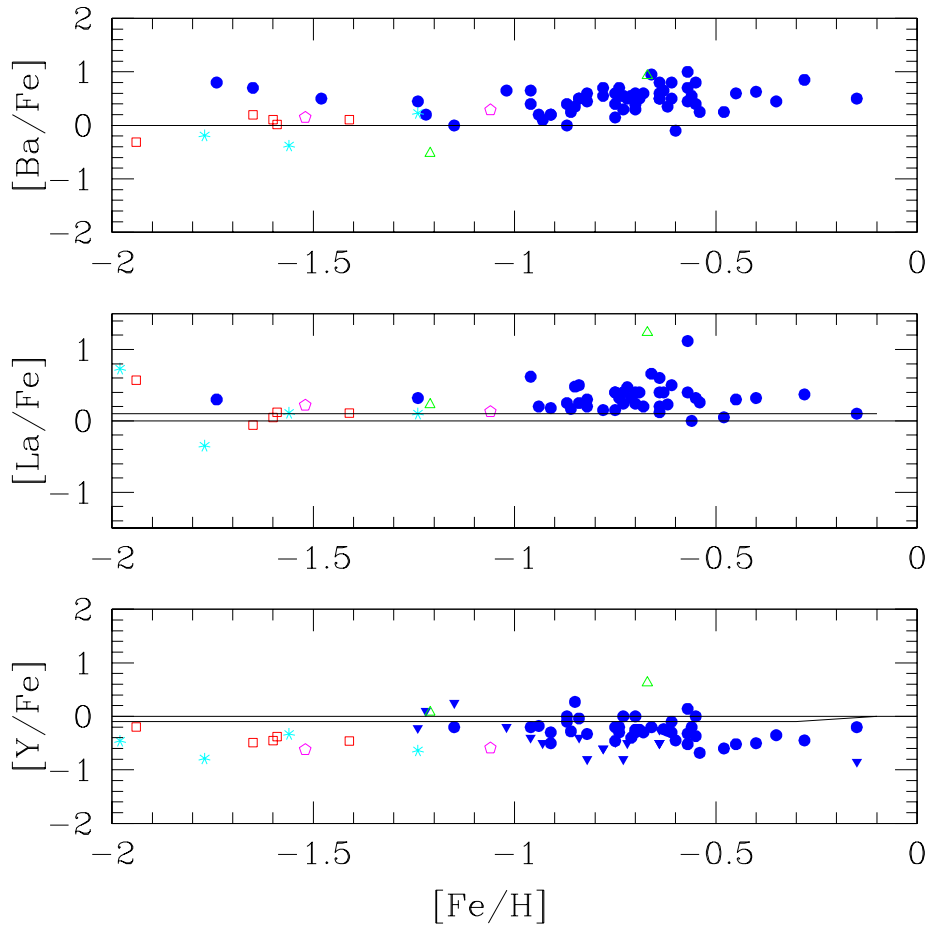


Fig. 18. Comparison of the Inner Disk LMC stars with stars from the dwarf spheroidal galaxies. 4. *s*-process elements (symbols are the same as in Fig. 15).

Table 1. Photometric Data

| Star Reference | 2MASS number | V | I | J | K |
|----------------|------------------|--------|--------|--------|--------|
| | | mag | mag | mag | mag |
| RGB_1055 | 05113508-7112309 | 17.599 | 16.219 | 15.070 | 14.172 |
| RGB_1105 | 05125047-7107463 | 17.661 | 16.170 | 14.972 | 13.952 |
| RGB_1118 | 05104862-7109301 | 17.628 | 16.278 | 15.298 | 14.258 |
| RGB_499 | 05130497-7115406 | 17.023 | 15.699 | 14.624 | 13.905 |
| RGB_512 | 05105703-7111340 | 16.994 | 15.539 | 14.452 | 13.489 |
| RGB_522 | 05112258-7107277 | 17.005 | 15.537 | 14.360 | 13.420 |
| RGB_533 | 05131266-7118005 | 16.958 | 15.537 | 14.562 | 13.571 |
| RGB_534 | 05123774-7118119 | 17.111 | 15.890 | 14.807 | 14.045 |
| RGB_546 | 05112068-7108113 | 17.041 | 15.619 | 14.546 | 13.639 |
| RGB_548 | 05130454-7113055 | 17.095 | 15.680 | 14.502 | 13.573 |
| RGB_564 | 05140580-7112054 | 17.127 | 15.935 | 14.887 | 14.235 |
| RGB_565 | 05111922-7112564 | 17.061 | 15.585 | 14.468 | 13.489 |
| RGB_576 | 05120852-7116597 | 17.132 | 15.806 | 14.668 | 13.631 |
| RGB_593 | 05132454-7109519 | 17.168 | 15.688 | 14.484 | 13.529 |
| RGB_599 | 05124460-7109195 | 17.174 | 15.756 | 14.574 | 13.663 |
| RGB_601 | 05111325-7120037 | 17.112 | 15.673 | 14.633 | 13.772 |
| RGB_606 | 05133509-7109322 | 17.152 | 15.791 | 14.694 | 13.850 |
| RGB_611 | 05114888-7111492 | 17.122 | 15.603 | 14.478 | 13.589 |
| RGB_614 | 05145465-7113031 | 17.023 | 15.492 | 14.459 | 13.375 |
| RGB_620 | 05142327-7107446 | 17.205 | 15.790 | 14.608 | 13.845 |
| RGB_625 | 05103395-7112074 | 17.144 | 15.614 | 14.473 | 13.440 |
| RGB_629 | 05104928-7110057 | 17.140 | 15.766 | 14.723 | 13.792 |
| RGB_631 | 05134131-7118477 | 17.054 | 15.655 | 14.638 | 13.638 |
| RGB_633 | 05120481-7113402 | 17.131 | 15.647 | 14.527 | 13.702 |
| RGB_640 | 05100529-7112259 | 17.154 | 15.772 | 14.747 | 13.791 |
| RGB_646 | 05140805-7117297 | 17.071 | 15.674 | 14.653 | 13.922 |
| RGB_651 | 05114466-7107176 | 17.152 | 15.713 | 14.672 | 13.729 |
| RGB_655 | 05143617-7109412 | 17.202 | 15.674 | 14.521 | 13.616 |
| RGB_656 | 05122551-7112106 | 17.191 | 15.758 | 14.637 | 13.743 |
| RGB_658 | 05100845-7109582 | 17.229 | 15.797 | 14.728 | 13.643 |
| RGB_664 | 05100659-7115514 | 17.156 | 15.529 | 14.438 | 13.336 |
| RGB_666 | 05104728-7119320 | 17.167 | 15.833 | 14.763 | 13.977 |
| RGB_671 | 05114880-7113428 | 17.197 | 15.705 | 14.555 | 13.585 |
| RGB_672 | 05130066-7116289 | 17.193 | 15.611 | 14.460 | 13.407 |

Table 1. Photometric Data

| Star Reference | 2MASS number | V | I | J | K |
|----------------|------------------|--------|--------|--------|--------|
| | | mag | mag | mag | mag |
| RGB_679 | 05123409-7113324 | 17.203 | 15.653 | 14.481 | 13.578 |
| RGB_690 | 05144229-7110108 | 17.266 | 15.678 | 14.488 | 13.413 |
| RGB_699 | 05095252-7115084 | 17.214 | 16.058 | 15.243 | 14.399 |
| RGB_700 | 05113581-7113336 | 17.284 | 15.821 | 14.717 | 13.676 |
| RGB_701 | 05124208-7110018 | 17.214 | 15.693 | 14.590 | 13.579 |
| RGB_705 | 05141536-7107463 | 17.215 | 15.886 | 14.866 | 14.026 |
| RGB_710 | 05110701-7108413 | 17.308 | 15.762 | 14.424 | 13.368 |
| RGB_720 | 05103055-7116158 | 17.314 | 15.984 | 14.901 | 14.313 |
| RGB_728 | 05142677-7119303 | 17.249 | 15.836 | 14.777 | 13.955 |
| RGB_731 | 05120180-7117002 | 17.255 | 15.593 | 14.382 | 13.357 |
| RGB_748 | 05122530-7119025 | 17.279 | 15.781 | 14.804 | 13.760 |
| RGB_752 | 05144969-7110095 | 17.320 | 15.801 | 14.566 | 13.621 |
| RGB_756 | 05143449-7112462 | 17.251 | 15.568 | 14.349 | 13.278 |
| RGB_758 | 05111461-7118573 | 17.269 | 15.983 | 14.996 | 14.266 |
| RGB_766 | 05111734-7115235 | 17.343 | 15.861 | 14.726 | 13.779 |
| RGB_773 | 05115657-7108489 | 17.264 | 15.707 | 14.632 | 13.602 |
| RGB_775 | 05095756-7116288 | 17.261 | 15.927 | 14.879 | 14.100 |
| RGB_776 | 05111615-7116401 | 17.287 | 15.877 | 14.826 | 14.033 |
| RGB_782 | 05104950-7107338 | 17.291 | 15.844 | 14.758 | 13.761 |
| RGB_789 | 05121657-7108570 | 17.310 | 15.629 | 14.382 | 13.267 |
| RGB_793 | 05110667-7111205 | 17.319 | 15.843 | 14.751 | 13.783 |
| RGB_808 | 05124558-7116301 | 17.360 | 16.105 | 15.141 | 14.450 |
| RGB_834 | 05112287-7116589 | 17.355 | 15.828 | - | - |
| RGB_854 | 05102155-7118506 | 17.415 | 15.997 | 14.922 | 14.064 |
| RGB_855 | 05124558-7116301 | 17.393 | 16.001 | 14.901 | 13.981 |
| RGB_859 | 05112287-7116589 | 17.397 | 15.883 | 14.730 | 13.806 |
| RGB_879 | 05144368-7114098 | 17.390 | 16.057 | - | - |
| RGB_900 | 05130400-7113289 | 17.400 | 15.983 | 14.915 | 14.032 |

Table 2. Stellar Parameters

| Star | T_{photLow} | T_{phot} | T_{spec} | $\log g_{\text{phot}}$ | $\log g_{\text{spec}}$ | $[\text{Fe}/\text{H}]_{\text{spec}}$ | $[\text{Fe}/\text{H}]_{\text{CaT}}$ | Vt | Rv |
|----------|----------------------|-------------------|-------------------|------------------------|------------------------|--------------------------------------|-------------------------------------|-----|-----|
| RGB_1055 | 4066 | 4118 | 4266 | 1.5 | 0.90 | -0.96 | -0.87 | 1.2 | 177 |
| RGB_1105 | 3921 | 3965 | 4100 | 1.4 | 0.90 | -0.75 | -1.15 | 1.6 | 243 |
| RGB_1118 | 4102 | 4154 | 4204 | 1.5 | 1.30 | -0.57 | -0.25 | 1.8 | 208 |
| RGB_499 | 4212 | 4269 | 4242 | 1.4 | 1.00 | -0.85 | -0.44 | 2.2 | 220 |
| RGB_512 | 4002 | 4051 | 4202 | 1.2 | 0.80 | -0.84 | -0.78 | 1.7 | 247 |
| RGB_522 | 3971 | 4016 | 4101 | 1.2 | 1.01 | -0.70 | -0.37 | 2.0 | 270 |
| RGB_533 | 4062 | 4113 | 4112 | 1.2 | 0.80 | -0.75 | -0.43 | 2.0 | 243 |
| RGB_534 | 4295 | 4359 | 4295 | 1.5 | 1.20 | -1.22 | -1.11 | 1.6 | 246 |
| RGB_546 | 4055 | 4107 | 4185 | 1.3 | 0.80 | -0.96 | -0.91 | 1.7 | 260 |
| RGB_548 | 4016 | 4064 | 4066 | 1.2 | 0.90 | -0.74 | -0.31 | 2.0 | 247 |
| RGB_564 | 4394 | 4463 | 4484 | 1.6 | 1.20 | -1.65 | -1.76 | 1.0 | 188 |
| RGB_565 | 3970 | 4016 | 4100 | 1.2 | 0.70 | -0.94 | -0.60 | 1.9 | 242 |
| RGB_576 | 4064 | 4117 | 4190 | 1.3 | 0.80 | -1.24 | -1.03 | 1.6 | 305 |
| RGB_593 | 3948 | 3993 | 4088 | 1.2 | 0.70 | -1.15 | -0.58 | 1.9 | 234 |
| RGB_599 | 4018 | 4066 | 4028 | 1.3 | 0.80 | -0.84 | -0.71 | 1.8 | 241 |
| RGB_601 | 4071 | 4123 | 4101 | 1.3 | 1.01 | -0.55 | -0.77 | 2.0 | 242 |
| RGB_606 | 4122 | 4174 | 4320 | 1.4 | 0.80 | -1.74 | -1.63 | 1.0 | 183 |
| RGB_611 | 3968 | 4010 | 3980 | 1.2 | 0.70 | -0.45 | -0.42 | 1.6 | 244 |
| RGB_614 | 3756 | 3967 | 4107 | 1.1 | 0.70 | -0.87 | -0.71 | 2.2 | 241 |
| RGB_620 | 4075 | 4127 | 4197 | 1.4 | 1.30 | -0.61 | -0.28 | 2.0 | 197 |
| RGB_625 | 3910 | 3951 | 4090 | 1.2 | 0.70 | -0.91 | -0.86 | 2.2 | 242 |
| RGB_629 | 4099 | 4150 | 4229 | 1.3 | 0.80 | -0.91 | -0.97 | 1.7 | 188 |
| RGB_631 | 4061 | 4112 | 4061 | 1.3 | 0.80 | -0.64 | -0.90 | 1.7 | 256 |
| RGB_633 | 4015 | 4067 | 4015 | 1.3 | 0.90 | -0.62 | -1.21 | 1.9 | 194 |
| RGB_640 | 4089 | 4141 | 4280 | 1.3 | 0.80 | -0.93 | -0.82 | 1.9 | 219 |
| RGB_646 | 4166 | 4218 | 4216 | 1.4 | 1.20 | -0.72 | -0.66 | 1.9 | 236 |
| RGB_651 | 4039 | 4091 | 4089 | 1.3 | 1.10 | -0.40 | -0.51 | 1.8 | 247 |
| RGB_655 | 3948 | 3988 | 4048 | 1.2 | 0.80 | -0.57 | -0.66 | 1.8 | 226 |
| RGB_656 | 4032 | 4084 | 4082 | 1.3 | 0.80 | -0.71 | -0.56 | 2.0 | 233 |
| RGB_658 | 3987 | 4033 | 4087 | 1.3 | 1.10 | -0.61 | -0.40 | 2.0 | 231 |
| RGB_664 | 3840 | 3881 | 3900 | 1.1 | 0.70 | -0.54 | -0.58 | 1.9 | 251 |
| RGB_666 | 4179 | 4233 | 4279 | 1.4 | 1.00 | -1.02 | -1.02 | 1.7 | 225 |
| RGB_671 | 3952 | 3996 | 4052 | 1.2 | 0.90 | -0.78 | -0.55 | 1.9 | 249 |
| RGB_672 | 3866 | 3906 | 3956 | 1.2 | 0.70 | -0.68 | -0.38 | 1.9 | 251 |
| RGB_679 | 3928 | 3968 | 3998 | 1.2 | 0.80 | -0.63 | -0.34 | 2.0 | 253 |

Table 2. continued

| Star | T_{photLow} | T_{phot} | T_{spec} | $\log g_{\text{phot}}$ | $\log g_{\text{spec}}$ | $[\text{Fe}/\text{H}]_{\text{spec}}$ | $[\text{Fe}/\text{H}]_{\text{CaT}}$ | Vt | Rv |
|---------|----------------------|-------------------|-------------------|------------------------|------------------------|--------------------------------------|-------------------------------------|-----|-----|
| RGB_690 | 3843 | 3883 | 3950 | 1.2 | 0.90 | -0.66 | -0.23 | 2.0 | 296 |
| RGB_699 | 4458 | 4531 | 4488 | 1.6 | 1.20 | -0.64 | -1.15 | 1.4 | 230 |
| RGB_700 | 3966 | 4011 | 4000 | 1.3 | 1.01 | -0.60 | -0.37 | 2.0 | 282 |
| RGB_701 | 3934 | 3975 | 4125 | 1.2 | 0.70 | -0.73 | -0.33 | 2.1 | 257 |
| RGB_705 | 4182 | 4237 | 4202 | 1.4 | 1.20 | -0.55 | -0.72 | 1.6 | 250 |
| RGB_710 | 3834 | 3870 | 3950 | 1.1 | 0.80 | -0.75 | -0.65 | 1.9 | 265 |
| RGB_720 | 3814 | 4320 | 4370 | 1.6 | 1.40 | -0.82 | -0.90 | 1.7 | 200 |
| RGB_728 | 4102 | 4153 | 4252 | 1.4 | 0.90 | -0.85 | -0.80 | 2.1 | 270 |
| RGB_731 | 3804 | 3844 | 3900 | 1.1 | 0.80 | -0.48 | -0.23 | 1.8 | 278 |
| RGB_748 | 3980 | 4026 | 4186 | 1.3 | 0.90 | -0.35 | -0.17 | 1.5 | 223 |
| RGB_752 | 3915 | 3956 | 3915 | 1.2 | 1.01 | -0.28 | -0.08 | 1.8 | 225 |
| RGB_756 | 3780 | 3813 | 3930 | 1.1 | 0.70 | -0.82 | -0.46 | 2.0 | 254 |
| RGB_758 | 4282 | 4347 | 4442 | 1.6 | 1.20 | -0.95 | -1.22 | 1.7 | 257 |
| RGB_766 | 3971 | 4016 | 4156 | 1.3 | 0.90 | -0.64 | -0.46 | 1.9 | 282 |
| RGB_773 | 3914 | 3954 | 4034 | 1.2 | 0.80 | -0.87 | -0.51 | 2.4 | 232 |
| RGB_775 | 4191 | 4245 | 4271 | 1.5 | 1.01 | -0.82 | -1.28 | 1.2 | 241 |
| RGB_776 | 4118 | 4170 | 4178 | 1.4 | 1.01 | -0.73 | -0.75 | 1.7 | 241 |
| RGB_782 | 3998 | 4045 | 4078 | 1.3 | 0.90 | -0.57 | -0.34 | 1.8 | 249 |
| RGB_789 | 3763 | 3796 | 3923 | 1.1 | 0.60 | -0.56 | -0.36 | 1.8 | 245 |
| RGB_793 | 3982 | 4029 | 4169 | 1.3 | 0.80 | -0.70 | -0.53 | 1.9 | 241 |
| RGB_808 | 4347 | 4412 | 4550 | 1.6 | 1.10 | -1.48 | -1.50 | 1.6 | 177 |
| RGB_834 | 3953 | 3993 | 4053 | 1.3 | 0.80 | -0.86 | -0.64 | 2.0 | 197 |
| RGB_854 | 4077 | 4129 | 4157 | 1.4 | 1.20 | -0.70 | -0.10 | 2.0 | 313 |
| RGB_855 | 4065 | 4117 | 4257 | 1.4 | 1.20 | -0.74 | -0.02 | 1.9 | 217 |
| RGB_859 | 3951 | 3992 | 4021 | 1.3 | 1.01 | -0.64 | -0.22 | 1.9 | 244 |
| RGB_879 | 4212 | 4273 | 4312 | 1.5 | 1.20 | -0.78 | -1.14 | 1.9 | 252 |
| RGB_900 | 4071 | 4123 | 4131 | 1.4 | 1.01 | -0.69 | -0.27 | 2.1 | 276 |

Table 3. Line List

| Wavelength | Element | χ_{exc} | log gf | Wavelength | Element | χ_{exc} | log gf |
|------------|---------|--------------|--------|------------|---------|--------------|--------|
| 6300.310 | O1 | 0.000 | -9.770 | 6355.040 | FE1 | 2.840 | -2.290 |
| 6274.660 | V1 | 0.270 | -1.670 | 6411.660 | FE1 | 3.650 | -0.720 |
| 6285.170 | V1 | 0.280 | -1.510 | 6301.510 | FE1 | 3.650 | -0.600 |
| 6199.190 | V1 | 0.290 | -1.290 | 6302.500 | FE1 | 3.690 | -0.910 |
| 6292.820 | V1 | 0.290 | -1.470 | 6336.830 | FE1 | 3.690 | -1.050 |
| 6224.510 | V1 | 0.290 | -2.010 | 6408.030 | FE1 | 3.690 | -1.000 |
| 6251.820 | V1 | 0.290 | -1.300 | 5809.220 | FE1 | 3.883 | -1.690 |
| 6150.150 | V1 | 0.300 | -1.790 | 6188.020 | FE1 | 3.940 | -1.720 |
| 6135.370 | V1 | 1.050 | -0.750 | 6157.730 | FE1 | 4.076 | -1.110 |
| 6119.530 | V1 | 1.060 | -0.320 | 6165.360 | FE1 | 4.142 | -1.470 |
| 6452.320 | V1 | 1.190 | -1.210 | 6380.750 | FE1 | 4.190 | -1.380 |
| 6531.410 | V1 | 1.218 | -0.840 | 5618.630 | FE1 | 4.209 | -1.260 |
| 6357.290 | V1 | 1.849 | -0.910 | 5638.270 | FE1 | 4.220 | -0.870 |
| 6435.010 | Y1 | 0.070 | -0.820 | 5635.820 | FE1 | 4.256 | -1.740 |
| 6496.900 | BA2 | 0.604 | -0.380 | 5641.450 | FE1 | 4.260 | -1.180 |
| 6572.800 | CA1 | 0.000 | -4.300 | 5814.810 | FE1 | 4.283 | -1.820 |
| 6162.190 | CA1 | 1.900 | -0.090 | 5717.830 | FE1 | 4.284 | -0.980 |
| 6169.560 | CA1 | 2.520 | -0.270 | 5705.470 | FE1 | 4.301 | -1.360 |
| 6169.040 | CA1 | 2.520 | -0.540 | 5691.500 | FE1 | 4.301 | -1.370 |
| 5601.290 | CA1 | 2.520 | -0.690 | 5619.610 | FE1 | 4.390 | -1.700 |
| 6493.790 | CA1 | 2.521 | 0.140 | 5806.730 | FE1 | 4.607 | -0.900 |
| 6166.440 | CA1 | 2.521 | -0.900 | 5679.020 | FE1 | 4.651 | -0.770 |
| 6499.650 | CA1 | 2.523 | -0.590 | 6597.560 | FE1 | 4.795 | -0.920 |
| 6161.300 | CA1 | 2.523 | -1.030 | 6469.190 | FE1 | 4.835 | -0.620 |
| 6455.610 | CA1 | 2.523 | -1.360 | 5633.950 | FE1 | 4.990 | -0.270 |
| 6439.080 | CA1 | 2.526 | 0.470 | 6516.080 | FE2 | 2.890 | -3.450 |
| 6471.670 | CA1 | 2.526 | -0.590 | 61432.68 | FE2 | 2.890 | -3.708 |
| 6508.840 | CA1 | 2.526 | -2.110 | 6149.250 | FE2 | 3.889 | -2.724 |
| 5647.240 | CO1 | 2.280 | -1.560 | 6247.560 | FE2 | 3.890 | -2.329 |
| 6330.100 | CR1 | 0.940 | -2.910 | 6416.920 | FE2 | 3.891 | -2.740 |
| 6362.880 | CR1 | 0.940 | -2.700 | 6456.390 | FE2 | 3.900 | -2.075 |
| 5787.930 | CR1 | 3.320 | -0.080 | 6320.430 | LA2 | 0.170 | -1.520 |
| 5783.070 | CR1 | 3.320 | -0.500 | 5711.090 | MG1 | 4.346 | -1.833 |
| 5782.130 | CU1 | 1.642 | -1.720 | 5688.220 | NA1 | 2.100 | -0.460 |

Table 3. continued.

| Wavelength | Element | χ_{exc} | log gf | Wavelength | Element | χ_{exc} | log gf |
|------------|---------|--------------|--------|------------|---------|--------------|--------|
| 6358.690 | FE1 | 0.860 | -4.470 | 5682.650 | NA1 | 2.100 | -0.700 |
| 6498.950 | FE1 | 0.960 | -4.700 | 6160.750 | NA1 | 2.100 | -1.230 |
| 6574.250 | FE1 | 0.990 | -5.020 | 6154.230 | NA1 | 2.100 | -1.530 |
| 6581.220 | FE1 | 1.480 | -4.860 | 6327.600 | NI1 | 1.680 | -3.150 |
| 6430.860 | FE1 | 2.180 | -2.010 | 6128.980 | NI1 | 1.680 | -3.330 |
| 6151.620 | FE1 | 2.180 | -3.300 | 6314.670 | NI1 | 1.930 | -1.770 |
| 6335.340 | FE1 | 2.200 | -2.180 | 6482.810 | NI1 | 1.930 | -2.630 |
| 6297.800 | FE1 | 2.220 | -2.740 | 6532.890 | NI1 | 1.935 | -3.390 |
| 6173.340 | FE1 | 2.220 | -2.880 | 6586.320 | NI1 | 1.950 | -2.810 |
| 6421.350 | FE1 | 2.279 | -2.010 | 6175.370 | NI1 | 4.090 | -0.530 |
| 6481.880 | FE1 | 2.280 | -2.980 | 5657.150 | SC2 | 1.500 | -0.603 |
| 6392.540 | FE1 | 2.280 | -4.030 | 5665.560 | SI1 | 4.920 | -1.720 |
| 6608.040 | FE1 | 2.280 | -4.030 | 5690.430 | SI1 | 4.930 | -1.870 |
| 6494.990 | FE1 | 2.400 | -1.270 | 5793.070 | SI1 | 4.930 | -2.060 |
| 6393.610 | FE1 | 2.430 | -1.580 | 6599.110 | TI1 | 0.900 | -2.085 |
| 6344.160 | FE1 | 2.430 | -2.920 | 6126.220 | TI1 | 1.070 | -1.420 |
| 6593.870 | FE1 | 2.437 | -2.420 | 6261.110 | TI1 | 1.430 | -0.480 |
| 5701.560 | FE1 | 2.560 | -2.220 | 6554.240 | TI1 | 1.440 | -1.220 |
| 6609.120 | FE1 | 2.560 | -2.690 | 6303.770 | TI1 | 1.440 | -1.570 |
| 6475.630 | FE1 | 2.560 | -2.940 | 6258.100 | TI1 | 1.443 | -0.350 |
| 6137.700 | FE1 | 2.590 | -1.400 | 6556.080 | TI1 | 1.460 | -1.080 |
| 6322.690 | FE1 | 2.590 | -2.430 | 5648.580 | TI1 | 2.490 | -0.250 |
| 6575.040 | FE1 | 2.590 | -2.710 | 6559.590 | TI2 | 2.048 | -2.190 |
| 6200.320 | FE1 | 2.610 | -2.440 | 6491.560 | TI2 | 2.061 | -1.793 |
| 6180.210 | FE1 | 2.730 | -2.650 | 6606.950 | TI2 | 2.061 | -2.790 |
| 6518.370 | FE1 | 2.830 | -2.300 | 6134.570 | ZR1 | 0.000 | -1.280 |

Table 4. Abundance ratios of the elements. Iron and Si, Ca, Ti1 and Ti2.

| Star | [Fe/H] | [Si/Fe] | [Ca/Fe] | [Ti1/Fe] | [Ti2/Fe] |
|----------|------------------|------------------|------------------|------------------|------------------|
| RGB_1055 | -0.96 ± 0.16 | -0.01 ± 0.15 | -0.10 ± 0.17 | -0.21 ± 0.18 | -0.06 ± 0.17 |
| RGB_1105 | -0.75 ± 0.16 | 0.05 ± 0.24 | -0.08 ± 0.20 | 0.14 ± 0.21 | 0.02 ± 0.16 |
| RGB_1118 | -0.57 ± 0.16 | 0.13 ± 0.20 | 0.03 ± 0.20 | 0.00 ± 0.18 | 0.13 ± 0.20 |
| RGB_499 | -0.85 ± 0.16 | 0.19 ± 0.18 | -0.03 ± 0.19 | 0.18 ± 0.18 | -0.05 ± 0.18 |
| RGB_512 | -0.84 ± 0.16 | -0.07 ± 0.16 | -0.06 ± 0.18 | 0.06 ± 0.18 | -0.04 ± 0.16 |
| RGB_522 | -0.70 ± 0.16 | 0.24 ± 0.17 | -0.13 ± 0.18 | 0.09 ± 0.17 | 0.22 ± 0.17 |
| RGB_533 | -0.75 ± 0.16 | 0.07 ± 0.22 | -0.08 ± 0.19 | 0.17 ± 0.18 | -0.06 ± 0.20 |
| RGB_534 | -1.22 ± 0.16 | 0.16 ± 0.18 | 0.00 ± 0.17 | 0.12 ± 0.18 | 0.13 ± 0.18 |
| RGB_546 | -0.96 ± 0.16 | -0.02 ± 0.20 | 0.05 ± 0.18 | -0.06 ± 0.18 | -0.04 ± 0.15 |
| RGB_548 | -0.74 ± 0.16 | 0.09 ± 0.17 | -0.26 ± 0.18 | 0.03 ± 0.18 | -0.08 ± 0.17 |
| RGB_564 | -1.65 ± 0.16 | 0.07 ± 0.30 | 0.05 ± 0.17 | 0.22 ± 0.26 | 0.53 ± 0.20 |
| RGB_565 | -0.94 ± 0.16 | -0.01 ± 0.15 | -0.12 ± 0.17 | 0.15 ± 0.17 | 0.00 ± 0.15 |
| RGB_576 | -1.24 ± 0.16 | -0.04 ± 0.17 | 0.00 ± 0.17 | -0.03 ± 0.17 | 0.05 ± 0.16 |
| RGB_593 | -1.15 ± 0.16 | 0.06 ± 0.18 | -0.04 ± 0.19 | 0.15 ± 0.18 | 0.00 ± 0.30 |
| RGB_599 | -0.84 ± 0.16 | 0.05 ± 0.19 | -0.14 ± 0.18 | -0.10 ± 0.18 | 0.06 ± 0.19 |
| RGB_601 | -0.55 ± 0.16 | 0.14 ± 0.19 | -0.22 ± 0.19 | -0.07 ± 0.18 | -0.06 ± 0.19 |
| RGB_606 | -1.74 ± 0.16 | - ± * | 0.13 ± 0.18 | -0.17 ± 0.19 | 0.21 ± 0.28 |
| RGB_611 | -0.45 ± 0.16 | -0.05 ± 0.18 | -0.12 ± 0.22 | 0.01 ± 0.19 | -0.14 ± 0.18 |
| RGB_614 | -0.87 ± 0.17 | - ± * | -0.07 ± 0.18 | 0.22 ± 0.18 | -0.01 ± 0.20 |
| RGB_620 | -0.61 ± 0.17 | 0.24 ± 0.22 | -0.23 ± 0.18 | 0.08 ± 0.20 | 0.28 ± 0.22 |
| RGB_625 | -0.91 ± 0.16 | 0.09 ± 0.15 | 0.15 ± 0.18 | 0.12 ± 0.18 | 0.09 ± 0.25 |
| RGB_629 | -0.91 ± 0.16 | -0.05 ± 0.16 | -0.19 ± 0.17 | -0.14 ± 0.17 | 0.06 ± 0.16 |
| RGB_631 | -0.64 ± 0.16 | 0.02 ± 0.20 | -0.03 ± 0.20 | -0.04 ± 0.18 | 0.06 ± 0.20 |
| RGB_633 | -0.62 ± 0.16 | -0.01 ± 0.19 | -0.21 ± 0.18 | -0.14 ± 0.18 | 0.06 ± 0.20 |
| RGB_640 | -0.93 ± 0.16 | 0.02 ± 0.18 | 0.08 ± 0.19 | -0.05 ± 0.18 | 0.07 ± 0.20 |
| RGB_646 | -1.37 ± 0.19 | 0.61 ± 0.49 | 0.48 ± 0.20 | 0.66 ± 0.20 | -0.10 ± 0.19 |
| RGB_651 | -0.40 ± 0.16 | 0.07 ± 0.20 | -0.31 ± 0.19 | -0.23 ± 0.18 | -0.11 ± 0.20 |
| RGB_655 | -0.57 ± 0.16 | 0.13 ± 0.18 | -0.24 ± 0.18 | -0.09 ± 0.18 | -0.02 ± 0.18 |
| RGB_656 | -0.71 ± 0.16 | 0.07 ± 0.17 | -0.07 ± 0.19 | 0.03 ± 0.20 | 0.02 ± 0.26 |
| RGB_658 | -0.61 ± 0.16 | - ± * | -0.24 ± 0.18 | -0.05 ± 0.18 | -0.06 ± 0.29 |
| RGB_664 | -0.54 ± 0.16 | 0.16 ± 0.20 | -0.45 ± 0.18 | -0.22 ± 0.19 | 0.00 ± 0.22 |
| RGB_666 | -1.02 ± 0.16 | -0.08 ± 0.18 | -0.08 ± 0.18 | -0.11 ± 0.19 | -0.06 ± 0.18 |
| RGB_671 | -0.78 ± 0.16 | 0.10 ± 0.17 | -0.11 ± 0.20 | -0.21 ± 0.17 | -0.06 ± 0.19 |
| RGB_672 | -0.68 ± 0.16 | 0.13 ± 0.20 | -0.11 ± 0.20 | 0.01 ± 0.18 | 0.12 ± 0.20 |
| RGB_679 | -0.63 ± 0.16 | 0.14 ± 0.18 | -0.19 ± 0.19 | -0.15 ± 0.19 | -0.08 ± 0.18 |

Table 4. continued.

| Star | [Fe/H] | [Si/Fe] | [Ca/Fe] | [Ti1/Fe] | [Ti2/Fe] |
|---------|------------------|------------------|------------------|------------------|------------------|
| RGB_690 | -0.66 ± 0.16 | 0.24 ± 0.17 | -0.27 ± 0.19 | 0.03 ± 0.18 | -0.10 ± 0.17 |
| RGB_699 | -0.64 ± 0.16 | 0.01 ± 0.21 | -0.05 ± 0.17 | -0.21 ± 0.17 | -0.04 ± 0.27 |
| RGB_700 | -0.60 ± 0.16 | 0.30 ± 0.19 | -0.36 ± 0.19 | -0.29 ± 0.18 | -0.10 ± 0.19 |
| RGB_701 | -0.73 ± 0.17 | 0.11 ± 0.24 | 0.19 ± 0.21 | 0.20 ± 0.19 | 0.00 ± 0.31 |
| RGB_705 | -0.55 ± 0.16 | 0.05 ± 0.17 | -0.08 ± 0.20 | -0.21 ± 0.18 | -0.03 ± 0.19 |
| RGB_710 | -0.75 ± 0.16 | 0.08 ± 0.17 | -0.28 ± 0.19 | -0.22 ± 0.18 | 0.01 ± 0.17 |
| RGB_720 | -0.82 ± 0.16 | 0.21 ± 0.18 | -0.06 ± 0.18 | 0.00 ± 0.18 | 0.16 ± 0.18 |
| RGB_728 | -0.85 ± 0.16 | 0.08 ± 0.18 | -0.02 ± 0.18 | 0.02 ± 0.18 | 0.35 ± 0.18 |
| RGB_731 | -0.48 ± 0.16 | -0.05 ± 0.20 | -0.28 ± 0.19 | -0.15 ± 0.19 | -0.09 ± 0.21 |
| RGB_748 | -0.35 ± 0.17 | -0.10 ± 0.24 | -0.14 ± 0.27 | 0.06 ± 0.21 | -0.29 ± 0.29 |
| RGB_752 | -0.28 ± 0.16 | 0.11 ± 0.18 | -0.36 ± 0.19 | -0.02 ± 0.19 | -0.01 ± 0.18 |
| RGB_756 | -0.82 ± 0.16 | 0.13 ± 0.18 | -0.11 ± 0.19 | 0.21 ± 0.19 | -0.01 ± 0.18 |
| RGB_758 | -0.95 ± 0.16 | $- \pm *$ | -0.11 ± 0.18 | -0.02 ± 0.20 | -0.05 ± 0.20 |
| RGB_766 | -0.64 ± 0.17 | 0.13 ± 0.24 | -0.18 ± 0.18 | 0.05 ± 0.18 | -0.02 ± 0.24 |
| RGB_773 | -0.91 ± 0.16 | 0.21 ± 0.21 | -0.29 ± 0.19 | 0.14 ± 0.18 | 0.20 ± 0.21 |
| RGB_775 | -0.82 ± 0.16 | -0.15 ± 0.17 | -0.11 ± 0.18 | -0.17 ± 0.18 | -0.10 ± 0.22 |
| RGB_776 | -0.73 ± 0.16 | -0.19 ± 0.16 | -0.13 ± 0.18 | -0.16 ± 0.18 | 0.03 ± 0.16 |
| RGB_782 | -0.57 ± 0.16 | 0.08 ± 0.21 | -0.24 ± 0.19 | -0.11 ± 0.18 | -0.07 ± 0.21 |
| RGB_789 | -0.56 ± 0.16 | 0.01 ± 0.18 | -0.24 ± 0.18 | 0.13 ± 0.19 | 0.04 ± 0.18 |
| RGB_793 | -0.70 ± 0.16 | -0.07 ± 0.18 | -0.16 ± 0.18 | -0.06 ± 0.18 | 0.01 ± 0.18 |
| RGB_808 | -1.48 ± 0.16 | 0.35 ± 0.18 | 0.03 ± 0.17 | -0.01 ± 0.19 | 0.20 ± 0.15 |
| RGB_834 | -0.86 ± 0.16 | -0.10 ± 0.17 | -0.21 ± 0.17 | 0.06 ± 0.19 | 0.11 ± 0.17 |
| RGB_854 | -1.32 ± 0.18 | 0.72 ± 0.38 | 0.51 ± 0.20 | 0.73 ± 0.23 | 0.05 ± 0.36 |
| RGB_855 | -0.74 ± 0.16 | 0.00 ± 0.21 | -0.13 ± 0.19 | 0.05 ± 0.18 | 0.11 ± 0.22 |
| RGB_859 | -0.97 ± 0.17 | 0.46 ± 0.23 | 0.20 ± 0.21 | 0.19 ± 0.18 | 0.09 ± 0.18 |
| RGB_879 | -0.78 ± 0.16 | -0.16 ± 0.22 | -0.20 ± 0.19 | 0.78 ± 0.17 | 0.29 ± 0.32 |
| RGB_900 | -0.69 ± 0.16 | 0.20 ± 0.20 | -0.12 ± 0.19 | -0.06 ± 0.18 | 0.09 ± 0.20 |

Table 5. Abundance ratios of the elements. Na, Sc, Cu and the α -elements Mg and O.

| Star | [O/Fe] | [Mg/Fe] | [Na/Fe] | [Sc/Fe] | [Cu/Fe] |
|----------|----------|---------|------------------|---------|---------|
| RGB_1055 | 0.10 | 0.50 | -0.76 ± 0.22 | 0.20 | -0.57 |
| RGB_1105 | - | 0.02 | -0.42 ± 0.20 | 0.04 | -0.78 |
| RGB_1118 | 0.10 | 0.00 | -0.28 ± 0.22 | -0.16 | -0.84 |
| RGB_499 | 0.40 | 0.15 | -0.06 ± 0.21 | -0.23 | -0.55 |
| RGB_512 | - | 0.32 | -0.42 ± 0.19 | 0.10 | -0.80 |
| RGB_522 | - | 0.40 | -0.03 ± 0.23 | -0.18 | -0.46 |
| RGB_533 | - | 0.30 | -0.08 ± 0.22 | -0.15 | -0.62 |
| RGB_534 | - | 0.28 | -0.23 ± 0.21 | -0.11 | -0.60 |
| RGB_546 | - | 0.10 | -0.43 ± 0.22 | 0.22 | -0.94 |
| RGB_548 | - | 0.25 | -0.29 ± 0.20 | 0.00 | -0.46 |
| RGB_564 | - | - | 0.09 ± 0.41 | - | - |
| RGB_565 | - | 0.32 | -0.16 ± 0.19 | -0.06 | -0.83 |
| RGB_576 | - | 0.31 | -0.27 ± 0.19 | 0.03 | -0.84 |
| RGB_593 | - | 0.50 | -0.27 ± 0.18 | 0.04 | -0.75 |
| RGB_599 | - | 0.30 | -0.41 ± 0.21 | -0.10 | -0.84 |
| RGB_601 | - | 0.33 | 0.10 ± 0.23 | -0.20 | -0.40 |
| RGB_606 | <-0.20 | - | 0.09 ± 0.30 | -0.10 | - |
| RGB_611 | - | 0.12 | -0.41 ± 0.22 | -0.26 | -0.90 |
| RGB_614 | <0.15 | - | -0.09 ± 0.26 | - | - |
| RGB_620 | <0.05 | 0.10 | 0.06 ± 0.25 | -0.12 | -0.30 |
| RGB_625 | - | 0.00 | -0.06 ± 0.19 | -0.20 | -0.80 |
| RGB_629 | 0.30 | 0.14 | -0.48 ± 0.20 | 0.00 | -0.90 |
| RGB_631 | - | 0.20 | -0.01 ± 0.22 | -0.03 | -0.68 |
| RGB_633 | 0.10 | - | -0.20 ± 0.21 | -0.50 | -0.50 |
| RGB_640 | - | 0.12 | -0.25 ± 0.23 | -0.20 | -0.85 |
| RGB_646 | - | 0.17 | 0.22 ± 0.38 | -0.22 | -0.80 |
| RGB_651 | - | 0.15 | -0.38 ± 0.22 | -0.20 | -0.44 |
| RGB_655 | - | 0.36 | -0.28 ± 0.23 | -0.10 | -0.80 |
| RGB_656 | - | 0.30 | -0.06 ± 0.21 | -0.30 | -0.64 |
| RGB_658 | - | - | -0.10 ± 0.24 | - | - |
| RGB_664 | - | 0.30 | -0.24 ± 0.22 | -0.30 | -0.90 |
| RGB_666 | - | 0.22 | -0.37 ± 0.19 | - | -0.85 |
| RGB_671 | - | - | -0.23 ± 0.20 | -0.10 | -0.50 |
| RGB_672 | - | 0.10 | -0.28 ± 0.22 | -0.33 | -0.64 |
| RGB_679 | - | 0.00 | -0.36 ± 0.21 | -0.37 | -0.70 |

Table 5. continued.

| Star | [O/Fe] | [Mg/Fe] | [Na/Fe] | [Sc/Fe] | [Cu/Fe] |
|---------|--------|---------|------------------|---------|---------|
| RGB_690 | - | 0.36 | -0.18 ± 0.21 | -0.23 | -0.68 |
| RGB_699 | - | 0.42 | -0.20 ± 0.22 | 0.00 | -0.80 |
| RGB_700 | <-0.05 | 0.10 | -0.31 ± 0.21 | <-0.20 | -0.67 |
| RGB_701 | - | 0.30 | 0.08 ± 0.25 | -0.04 | -0.50 |
| RGB_705 | - | 0.26 | -0.15 ± 0.20 | -0.19 | -0.75 |
| RGB_710 | - | 0.30 | -0.54 ± 0.20 | -0.08 | -0.58 |
| RGB_720 | <0.35 | 0.20 | -0.29 ± 0.21 | <-0.30 | - |
| RGB_728 | - | 0.11 | -0.33 ± 0.21 | -0.20 | -0.75 |
| RGB_731 | 0.00 | 0.03 | -0.56 ± 0.22 | -0.32 | -0.76 |
| RGB_748 | <0.00 | 0.20 | -0.38 ± 0.27 | 0.00 | -0.60 |
| RGB_752 | - | 0.20 | -0.28 ± 0.22 | -0.27 | -0.53 |
| RGB_756 | - | 0.05 | -0.25 ± 0.21 | <-0.30 | -0.75 |
| RGB_758 | - | - | 0.08 ± 0.26 | - | - |
| RGB_766 | <0.10 | 0.00 | -0.09 ± 0.25 | - | -0.50 |
| RGB_773 | 0.25 | 0.02 | 0.02 ± 0.23 | -0.32 | -0.57 |
| RGB_775 | - | 0.20 | -0.42 ± 0.20 | 0.14 | -0.83 |
| RGB_776 | - | 0.12 | -0.53 ± 0.20 | -0.13 | -0.80 |
| RGB_782 | - | 0.30 | -0.19 ± 0.22 | -0.28 | -0.80 |
| RGB_789 | - | 0.04 | -0.28 ± 0.22 | -0.30 | -0.74 |
| RGB_793 | <0.10 | 0.08 | -0.39 ± 0.21 | -0.30 | -0.80 |
| RGB_808 | 0.30 | 0.10 | -0.42 ± 0.19 | -0.02 | <-1.00 |
| RGB_834 | - | 0.13 | -0.32 ± 0.20 | -0.25 | -0.76 |
| RGB_854 | - | 0.30 | 0.40 ± 0.36 | -0.10 | -0.50 |
| RGB_855 | - | 0.10 | -0.17 ± 0.22 | -0.20 | -0.38 |
| RGB_859 | - | 0.22 | 0.12 ± 0.26 | -0.22 | -0.42 |
| RGB_879 | - | 0.22 | -0.29 ± 0.22 | - | - |
| RGB_900 | - | 0.34 | -0.13 ± 0.22 | -0.15 | -0.68 |

Table 6. Abundance ratios of the elements (continuation). FeII and Iron-peak elements.

| Star | [Cr/Fe] | [V/Fe] | [Ni/Fe] | [Co/Fe] |
|----------|--------------|--------------|--------------|---------|
| RGB_1055 | -0.47 ± 0.20 | -0.40 ± 0.18 | -0.32 ± 0.10 | <0.00 |
| RGB_1105 | -0.30 ± 0.19 | -0.04 ± 0.18 | -0.25 ± 0.10 | -0.10 |
| RGB_1118 | -0.19 ± 0.21 | -0.19 ± 0.19 | -0.20 ± 0.09 | -0.20 |
| RGB_499 | 0.11 ± 0.20 | 0.16 ± 0.18 | -0.21 ± 0.11 | -0.08 |
| RGB_512 | -0.18 ± 0.19 | 0.06 ± 0.19 | -0.15 ± 0.09 | -0.05 |
| RGB_522 | -0.08 ± 0.19 | 0.17 ± 0.18 | -0.07 ± 0.08 | -0.12 |
| RGB_533 | -0.13 ± 0.20 | 0.15 ± 0.19 | -0.23 ± 0.10 | -0.10 |
| RGB_534 | -0.25 ± 0.17 | 0.03 ± 0.18 | -0.11 ± 0.08 | 0.00 |
| RGB_546 | -0.18 ± 0.20 | -0.12 ± 0.18 | -0.28 ± 0.09 | -0.10 |
| RGB_548 | -0.28 ± 0.18 | -0.07 ± 0.18 | -0.27 ± 0.10 | -0.19 |
| RGB_564 | -0.03 ± 0.29 | 0.56 ± 0.22 | -0.26 ± 0.15 | - |
| RGB_565 | -0.18 ± 0.19 | 0.19 ± 0.18 | -0.20 ± 0.07 | -0.10 |
| RGB_576 | -0.43 ± 0.18 | -0.14 ± 0.18 | -0.14 ± 0.07 | 0.05 |
| RGB_593 | -0.24 ± 0.21 | 0.00 ± 0.18 | -0.24 ± 0.09 | -0.05 |
| RGB_599 | -0.24 ± 0.20 | -0.23 ± 0.18 | -0.26 ± 0.11 | -0.10 |
| RGB_601 | -0.08 ± 0.20 | 0.08 ± 0.19 | -0.21 ± 0.09 | -0.18 |
| RGB_606 | 0.35 ± 0.22 | 0.91 ± 0.40 | -0.46 ± 0.10 | <0.10 |
| RGB_611 | -0.18 ± 0.19 | -0.03 ± 0.19 | -0.28 ± 0.07 | -0.36 |
| RGB_614 | -0.17 ± 0.25 | 0.24 ± 0.19 | -0.41 ± 0.13 | - |
| RGB_620 | -0.07 ± 0.24 | 0.11 ± 0.19 | -0.16 ± 0.14 | <0.00 |
| RGB_625 | -0.11 ± 0.20 | 0.18 ± 0.19 | -0.18 ± 0.14 | 0.10 |
| RGB_629 | -0.45 ± 0.20 | -0.35 ± 0.18 | -0.24 ± 0.13 | <-0.20 |
| RGB_631 | -0.12 ± 0.20 | -0.03 ± 0.19 | -0.26 ± 0.10 | -0.14 |
| RGB_633 | -0.20 ± 0.20 | -0.06 ± 0.18 | -0.23 ± 0.09 | -0.04 |
| RGB_640 | -0.14 ± 0.21 | -0.02 ± 0.18 | -0.08 ± 0.09 | <-0.20 |
| RGB_646 | 0.28 ± 0.37 | 0.55 ± 0.20 | 0.46 ± 0.13 | -0.10 |
| RGB_651 | -0.28 ± 0.20 | -0.16 ± 0.19 | -0.26 ± 0.10 | -0.15 |
| RGB_655 | -0.09 ± 0.20 | 0.12 ± 0.18 | -0.13 ± 0.10 | -0.20 |
| RGB_656 | -0.21 ± 0.19 | 0.02 ± 0.18 | -0.25 ± 0.12 | -0.09 |
| RGB_658 | -0.56 ± 0.23 | 0.16 ± 0.19 | -0.04 ± 0.11 | - |
| RGB_664 | -0.29 ± 0.21 | -0.24 ± 0.19 | -0.36 ± 0.13 | -0.27 |
| RGB_666 | -0.43 ± 0.17 | -0.38 ± 0.18 | -0.27 ± 0.09 | - |
| RGB_671 | -0.28 ± 0.19 | -0.08 ± 0.18 | -0.23 ± 0.10 | -0.09 |
| RGB_672 | -0.11 ± 0.21 | 0.15 ± 0.18 | -0.21 ± 0.10 | -0.22 |
| RGB_679 | -0.25 ± 0.21 | -0.02 ± 0.18 | -0.28 ± 0.09 | -0.14 |

Table 6. continued.

| Star | [Cr/Fe] | [V/Fe] | [Ni/Fe] | [Co/Fe] |
|---------|------------------|------------------|------------------|---------|
| RGB_690 | -0.12 ± 0.19 | 0.01 ± 0.19 | -0.19 ± 0.08 | -0.22 |
| RGB_699 | -0.32 ± 0.20 | -0.42 ± 0.18 | -0.38 ± 0.10 | -0.17 |
| RGB_700 | -0.48 ± 0.20 | -0.20 ± 0.19 | -0.34 ± 0.12 | -0.20 |
| RGB_701 | 0.03 ± 0.23 | 0.23 ± 0.19 | -0.12 ± 0.16 | -0.12 |
| RGB_705 | -0.39 ± 0.21 | -0.18 ± 0.18 | -0.23 ± 0.10 | -0.25 |
| RGB_710 | -0.34 ± 0.20 | -0.31 ± 0.18 | -0.32 ± 0.10 | -0.20 |
| RGB_720 | -0.13 ± 0.19 | 0.04 ± 0.18 | -0.16 ± 0.15 | -0.29 |
| RGB_728 | -0.17 ± 0.20 | -0.28 ± 0.19 | -0.20 ± 0.14 | -0.08 |
| RGB_731 | -0.17 ± 0.20 | -0.14 ± 0.19 | -0.26 ± 0.07 | -0.20 |
| RGB_748 | 0.04 ± 0.24 | 0.35 ± 0.18 | -0.43 ± 0.13 | -0.10 |
| RGB_752 | -0.18 ± 0.19 | -0.15 ± 0.19 | -0.31 ± 0.11 | -0.13 |
| RGB_756 | -0.17 ± 0.19 | 0.25 ± 0.18 | -0.24 ± 0.10 | -0.10 |
| RGB_758 | -0.27 ± 0.25 | -0.08 ± 0.20 | -0.34 ± 0.13 | - |
| RGB_766 | -0.05 ± 0.23 | 0.25 ± 0.19 | -0.08 ± 0.09 | -0.09 |
| RGB_773 | -0.20 ± 0.21 | -0.05 ± 0.20 | -0.32 ± 0.13 | -0.01 |
| RGB_775 | -0.36 ± 0.21 | -0.34 ± 0.17 | -0.28 ± 0.09 | -0.22 |
| RGB_776 | -0.21 ± 0.21 | -0.26 ± 0.18 | -0.27 ± 0.09 | -0.22 |
| RGB_782 | -0.13 ± 0.21 | -0.19 ± 0.19 | -0.22 ± 0.08 | - |
| RGB_789 | -0.19 ± 0.19 | 0.28 ± 0.18 | -0.21 ± 0.09 | -0.20 |
| RGB_793 | -0.19 ± 0.20 | -0.14 ± 0.18 | -0.29 ± 0.09 | -0.20 |
| RGB_808 | -0.04 ± 0.25 | 0.13 ± 0.23 | -0.19 ± 0.15 | <0.10 |
| RGB_834 | -0.13 ± 0.19 | 0.05 ± 0.18 | -0.26 ± 0.10 | - |
| RGB_854 | 0.47 ± 0.35 | 0.56 ± 0.21 | 0.54 ± 0.12 | 0.12 |
| RGB_855 | -0.07 ± 0.21 | -0.04 ± 0.20 | -0.36 ± 0.14 | -0.04 |
| RGB_859 | -0.04 ± 0.24 | 0.28 ± 0.19 | 0.18 ± 0.09 | -0.08 |
| RGB_879 | -0.44 ± 0.21 | -0.21 ± 0.19 | -0.30 ± 0.15 | <-0.10 |
| RGB_900 | -0.14 ± 0.20 | -0.03 ± 0.18 | -0.18 ± 0.09 | -0.12 |

Table 7. Abundance ratios of the elements (continuation). Heavy and light *s*-process elements.

| Star | [La/Fe] | [Ba/Fe] | [Y/Fe] | [Zr/Fe] | Star | [La/Fe] | [Ba/Fe] | [Y/Fe] | [Zr/Fe] |
|----------|---------|---------|--------|---------|---------|---------|---------|--------|---------|
| RGB_1055 | <0.05 | 0.40 | <-0.40 | - | RGB_666 | <0.10 | 0.65 | <-0.20 | <-0.30 |
| RGB_1105 | 0.15 | 0.40 | <-0.48 | -0.50 | RGB_671 | 0.15 | 0.70 | <-0.60 | -0.65 |
| RGB_1118 | 1.12 | 1.00 | 0.14 | 0.00 | RGB_672 | 0.20 | 0.60 | -0.30 | -0.62 |
| RGB_499 | 0.48 | 0.35 | 0.27 | 0.00 | RGB_679 | 0.40 | 0.65 | -0.24 | -0.60 |
| RGB_512 | 0.50 | 0.50 | -0.04 | -0.17 | RGB_690 | 0.66 | 0.95 | -0.20 | -0.32 |
| RGB_522 | 0.40 | 0.60 | 0.00 | -0.35 | RGB_699 | 0.12 | 0.60 | <-0.50 | -0.80 |
| RGB_533 | 0.40 | 0.15 | -0.20 | -0.38 | RGB_700 | <0.30 | -0.10 | -0.45 | -0.90 |
| RGB_534 | <0.20 | 0.20 | <0.10 | <-0.35 | RGB_701 | 0.24 | 0.30 | 0.00 | -0.24 |
| RGB_546 | 0.62 | 0.65 | -0.20 | -0.20 | RGB_705 | 0.32 | 0.40 | -0.37 | -0.80 |
| RGB_548 | 0.32 | 0.70 | -0.30 | -0.61 | RGB_710 | 0.40 | 0.60 | -0.46 | -0.78 |
| RGB_564 | - | 0.70 | - | - | RGB_720 | - | 0.35 | - | -0.60 |
| RGB_565 | 0.20 | 0.20 | -0.18 | -0.30 | RGB_728 | <0.10 | 0.50 | -0.20 | <-0.50 |
| RGB_576 | 0.32 | 0.45 | <-0.20 | -0.28 | RGB_731 | 0.05 | 0.25 | -0.60 | -0.70 |
| RGB_593 | <0.20 | 0.00 | -0.20 | <-0.45 | RGB_748 | <-0.30 | 0.4 | -0.3 | <-0.8 |
| RGB_599 | 0.25 | 0.50 | <-0.40 | -0.40 | RGB_752 | 0.37 | 0.85 | -0.45 | -0.75 |
| RGB_601 | - | 0.80 | 0.00 | -0.43 | RGB_756 | 0.20 | 0.45 | -0.33 | -0.40 |
| RGB_606 | 0.30 | 0.80 | - | - | RGB_758 | - | - | - | - |
| RGB_611 | 0.30 | 0.60 | -0.52 | -0.70 | RGB_766 | 0.60 | 0.50 | <-0.25 | <-1.00 |
| RGB_614 | - | 0.40 | 0.00 | - | RGB_773 | 0.25 | 0.00 | -0.10 | -0.42 |
| RGB_620 | <0.50 | 0.50 | -0.10 | <-0.40 | RGB_775 | 0.30 | 0.60 | <-0.80 | -0.40 |
| RGB_625 | 0.18 | 0.20 | -0.30 | -0.24 | RGB_776 | 0.40 | 0.55 | <-0.80 | -0.84 |
| RGB_629 | <0.00 | 0.20 | -0.50 | <-0.60 | RGB_782 | <0.10 | 0.45 | -0.52 | -0.87 |
| RGB_631 | 0.20 | 0.50 | <-0.50 | <-1.00 | RGB_789 | 0.00 | 0.55 | -0.20 | -0.60 |
| RGB_633 | 0.23 | 0.35 | -0.27 | -0.55 | RGB_793 | 0.24 | 0.30 | -0.30 | -0.49 |
| RGB_640 | <0.10 | 0.10 | <-0.50 | <-0.20 | RGB_808 | <0.20 | 0.50 | - | - |
| RGB_646 | 0.47 | 0.50 | <-0.50 | <-0.40 | RGB_834 | 0.17 | 0.25 | -0.28 | -0.40 |
| RGB_651 | 0.32 | 0.63 | -0.50 | -0.77 | RGB_854 | <0.35 | 0.40 | -0.25 | -0.50 |
| RGB_655 | 0.40 | 0.70 | -0.32 | -0.38 | RGB_855 | - | 0.55 | -0.20 | -0.50 |
| RGB_656 | 0.32 | 0.55 | -0.40 | -0.60 | RGB_859 | 0.40 | 0.80 | <-0.50 | -0.56 |
| RGB_658 | - | 0.80 | -0.30 | - | RGB_879 | - | 0.55 | <-0.60 | - |
| RGB_664 | 0.26 | 0.25 | -0.68 | -0.80 | RGB_900 | 0.40 | 0.50 | -0.25 | -0.55 |

Table 8. Errors due to stellar parameters uncertainties.

| Element | $\Delta T_{\text{eff}}=+100$ K | $\Delta \log g=-0.4$ | $\Delta V_t=+0.2$ km/s | $\Delta [\text{Fe}/\text{H}]=-0.15$ | δ_{tot} |
|------------|--------------------------------|----------------------|------------------------|-------------------------------------|----------------|
| [Fe I/H] | -0.01 | -0.10 | -0.12 | -0.03 | 0.16 |
| [O I/Fe] | 0.04 | -0.06 | 0.10 | -0.02 | 0.12 |
| [V I/Fe] | 0.16 | 0.06 | 0.00 | 0.04 | 0.17 |
| [Y I/Fe] | 0.19 | 0.08 | 0.07 | 0.04 | 0.22 |
| [Ca I/Fe] | 0.11 | 0.11 | -0.01 | 0.04 | 0.16 |
| [Cr I/Fe] | 0.12 | 0.07 | 0.00 | 0.04 | 0.15 |
| [Fe II/Fe] | -0.18 | -0.16 | 0.08 | -0.07 | 0.26 |
| [Mg I/Fe] | 0.01 | 0.06 | 0.01 | 0.01 | 0.06 |
| [Na I/Fe] | 0.11 | 0.10 | 0.06 | 0.05 | 0.17 |
| [Ni I/Fe] | 0.01 | -0.03 | 0.05 | -0.01 | 0.06 |
| [Si I/Fe] | -0.07 | -0.01 | 0.09 | -0.01 | 0.12 |
| [Ti I/Fe] | 0.15 | 0.08 | 0.01 | 0.04 | 0.17 |
| [Ti II/Fe] | -0.05 | -0.10 | 0.04 | -0.04 | 0.12 |
| [Zr I/Fe] | 0.19 | 0.06 | 0.03 | 0.03 | 0.20 |
| [Ba II/Fe] | 0.04 | -0.04 | -0.04 | 0.00 | 0.07 |
| [Co I/Fe] | 0.03 | -0.01 | 0.05 | -0.01 | 0.06 |
| [Cu I/Fe] | 0.07 | -0.04 | 0.06 | 0.07 | 0.12 |
| [La II/Fe] | 0.04 | -0.06 | 0.05 | -0.04 | 0.10 |
| [Sc II/Fe] | -0.01 | -0.04 | 0.01 | -0.01 | 0.04 |